Direct observation of electronic structure in Se substituted La(O,F)BiS$_{2-x}$Se$_x$ by synchrotron ARPES

N. Kataoka[a], K. Hoshi[b], Y. Mizuguchi[b], M. Arita[c], K. Shimada[c],
T. Wakita[a, d] and T. Yokoya[a, d]

[a]*Graduate School Of Natural Science And Technology, Okayama University, Japan*
[b]*Department of Physics, Tokyo Metropolitan University, Japan*
[c]*Hiroshima Synchrotron Radiation Center, Hiroshima University, Japan*
[d]*Research Institute for Interdisciplinary Science, Okayama University, Japan*

Keywords: BiS$_2$-based superconductor, local atomic disorder, spin-orbit coupling, ARPES

BiCh_2 compounds are quasi-two-dimensional materials with a layered structure typically represented by the composition of RO$_{1-x}$F$_x$BiCh_2 (R=rare earth; Ch=S, Se). Electron carriers can be doped by replacing oxygen with fluorine atoms. Electron-doped samples show superconductivity below 2-10 K. Several experimental and theoretical studies have indicated the possibility of unconventional superconducting mechanisms [1]. The superconducting transition temperature is sensitive to the pressure applied to the BiCh_2 planes. Extended X-ray absorption fine structure (EXAFS) and other studies have suggested a scenario in which superconductivity is induced by the suppression of disorder [2, 3]. On the other hand, there are few reports of systematic studies on disorder and electronic structure. In this study, we performed angle-resolved photoemission spectroscopy (ARPES) measurements of LaO$_{0.5}$F$_{0.5}$BiS$_{2-x}$Se$_x$, a typical BiCh_2-based superconductor, to investigate the relationship between the disorder and electronic structure of BiCh_2.

LaO$_{0.5}$F$_{0.5}$BiS$_{2-x}$Se$_x$ ($x = 0$, 0.5, 1.0) single crystals were grown using a high-temperature flux method in a quartz tube in vacuum [4]. ARPES measurements were performed at BL-9A in Hiroshima Synchrotron Radiation Center (HiSOR) using an R4000 electron analyzer (Scienta Omicron) with p-polarized light. The total energy resolution was set to approximately 30 meV for $hv = 30$ eV. All samples were cleaved *in-situ* on the (001) plane in an ultrahigh vacuum of less than 5×10^{-9} Pa. All the measurements were performed at the same temperature of 13 K. The binding energies of samples were determined by referencing the Fermi energy (E_F) of gold electronically contacted with samples.

Figures 1(a), (b), and (c) show valence band ARPES intensity plots and momentum distribution curves (MDCs) at $E_\mathrm{F} \pm 5$ meV obtained from LaO$_{0.5}$F$_{0.5}$BiS$_{2-x}$Se$_x$ ($x = 0$, 0.5, and 1.0) measured along the Γ-X high symmetry direction in the Brillouin zone, respectively. The electronic band dispersions appear very similar with each other, in spite of the different energies of the bottom of the conduction band and the top of the valence band in each sample. On the other hand, if we focus on the band gap (E_g) at the X point, E_g decreases as x increases. This is due to the increase of bandwidth by Se substitution. For $x = 0.5$ and 1.0 samples, the conduction band splits clearly in the wavenumber direction. In contrast, the splitting is not so clear for $x = 0$. This splitting has been discussed as being due to the spin-orbit coupling (SOC) [5], which is weaker at $x = 0$ because the atomic mass of S is lighter than that of Se. Furthermore, the photoelectron intensity near-E_F seems to increase with increasing x. To evaluate the x dependence of photoelectron intensity near-E_F, momentum-integrated spectra of the conduction band near the X point were obtained. For $x = 0$, the photoelectron intensity near-E_F is strongly suppressed. However, for $x = 0.5$ and 1.0, the photoelectron intensity near-E_F increases, depending on the x values. This systematic change in the photoelectron intensity near-E_F is related to the disorder of the local atomic structure in the BiS$_2$-plane, which is known to be suppressed by Se substitution. In the future, we plan to conduct a detailed analysis by comparing the Fermi surface geometry and band calculations.
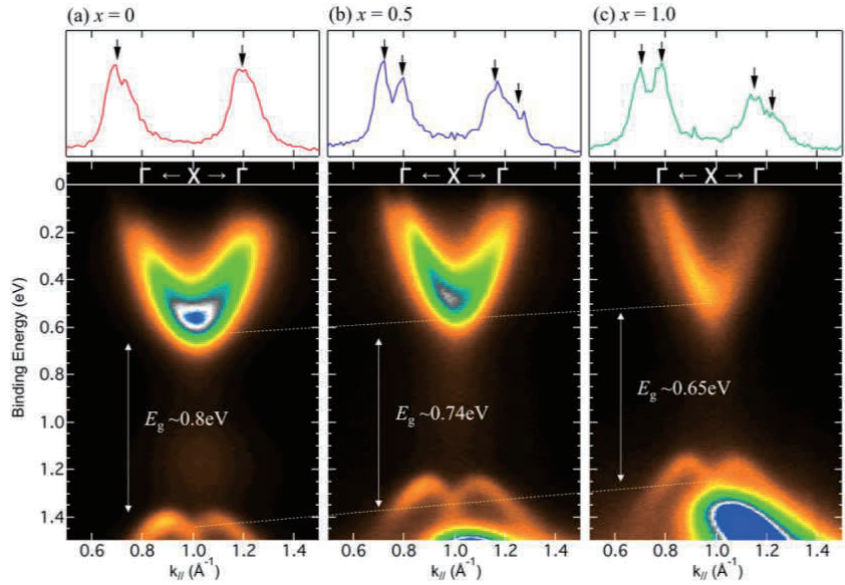
FIGURE 1. (a)-(c) ARPES results and MDC spectra at E_F for $LaO_{0.5}F_{0.5}BiS_{2-x}Se_x$ ($x = 0, 0.5, 1.0$), respectively. Shown in the form of the original ARPES spectrum (lower panel) and MDC spectrum (upper panel). The white dashed lines are guidelines for the bottom of the conduction band and the top of the valence band.
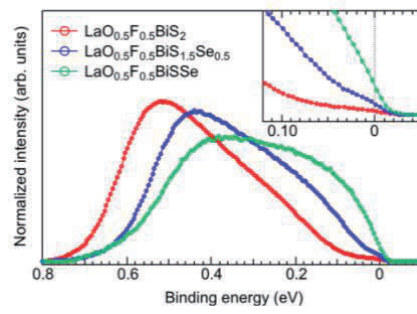

FIGURE 2. Momentum-integrated spectra of $LaO_{0.5}F_{0.5}BiS_{2-x}Se_x$ ($x = 0, 0.5, 1.0$). The inset shows an expanded view of the E_F region. The spectra were normalized by area after subtracting the Shirley background.

REFERENCES

1. Y. Mizuguchi J. Phys. Soc. Jpn. **88**, 041001 (2019).
2. Y. Mizuguchi *et al.*, Phys. Chem. Chem. Phys. **17**, 22090 (2015).
3. E. Paris *et al.,* J. Phys.: Condens. Matter **29**, 145603 (2017).
4. M. Nagao *et al.*, Nov. Supercond. Mater. **1**, 64 (2015).
5. K. Terashima *et al.*, Phys. Rev. B **90**, 220512(R) (2014).

Angle-resolved photoemission study of MnSi

M. Arita and K. Shimada

Hiroshima Synchrotron Radiation Center, Hiroshima University,
Kagamiyama, Higashi-Hiroshima 739-0046, Japan

Keywords: MnSi,ARPES,

The 3d transition metal monosilicides (MnSi, FeSi, and CoSi) have a cubic B20-type nonsymmorphic crystal structure (space grope No.198). These materials and their solid solutions have anomalous electrical and magnetic properties, which have attracted much interest for decades [1-3]. Among them, MnSi has a helical magnetic order below 29 K under zero magnetic fields. Under ~ 0.2 T magnetic field, the conical and skyrmion lattice phases appear below 28 K and between 28 and 29 K, respectively [4]. The origin of these magnetic phases is the breaking of the lattice inversion symmetry.

In this study, we report the electronic band structures of MnSi investigated using angle-resolved photoemission spectroscopy (ARPES). The MnSi single crystals were grown by the flux method with Ga flux and ARPES measurements were performed at HiSOR BL-9A. The clean surface of the MnSi [001] was obtained by mechanical polishing in air, 2 kV Ar-ion sputtering, and 760°C annealing in the UHV chamber. After that procedure, the clear 1×1 LEED images were seen for the [001] surfaces (Fig. 1).

Figure 2(a) shows the band structure of MnSi from ARPES measurements scanning along $\bar{\Gamma} - \bar{X}$ in the surface Brillouin Zone (BZ) with hv= 40 eV at 15 K. The wide dispersive structures are observed between the Fermi level (E_F) and E = -3 eV, which are derived from Mn 3d and Si 2p hybridized states. Assuming the inner potential V_0 of 10 eV, the electronic structure near the X-M line in the bulk BZ can be probed with this ARPES experimental condition [5]. For the comparison, we show the band dispersions along the X-M direction given by the GGA calculation in Fig. 2(b). The observed band structure is in qualitative agreement with the calculation result. The bandwidth of the observed valence band is almost the same as that of the calculated one. It is in contrast to the case of FeSi which is known as a 3d Kondo insulator. The valence bandwidth of FeSi as observed in the ARPES measurements shrank about 70% and the strong renormalized band near EF appeared below 50 K [6]. As these phenomena were not observed in MnSi, the electron correlation effect is not strong.

FIGURE 1. LEED image of the clean MnSi [001] surface which was obtained by mechanical polishing, and repeated Ar-ion sputtering and annealing in ultrahigh vacuum. The electron beam energy was E = 100 eV.
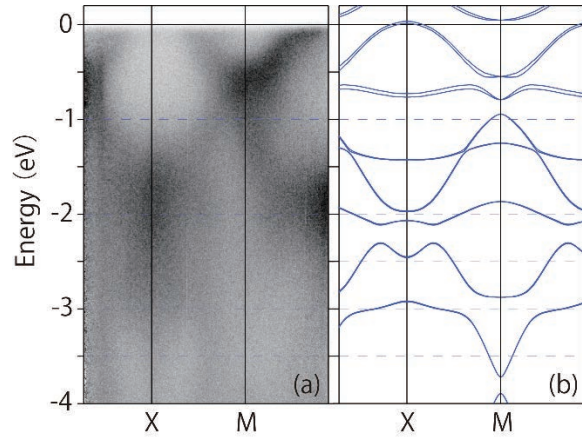
FIGURE 2. (a) ARPES intensity plot taken at $h\nu$= 30 eV. (b) Theoretical band dispersions along the X-M direction given by the GGA calculation.

REFERENCES

1.   V. Jaccarino et al., Phys Rev. 160, 476 (1967).
2.   J. H. Wernick et al., Mat. Res. Bull. 7, 1431 (1972).
3.   Y. Ishikawa et al., Phys. Rev. B 16, 4956 (1977).
4.   Y. Nii et al., Nat. Commun. 6, 8539 (2015).
5.   K. Kura et al., J. Phys. Soc. Jpn. 77, 024709 (2008).
6.   M. Arita et al., Phys. Rev. B 77, 205117 (2008).

Spin-Orbit-Induced Splitting of the Tamm Surface State of Re(0001)

Marcel Holtmann[a], Peter Krüger[b], Koji Miyamoto[c], Taichi Okuda[c], Pascal J. Grenz[a], Shiv Kumar[c], Kenya Shimada[c], and Markus Donath[a]

[a]*Physikalisches Institut, Westfälische Wilhelms-Universität Münster, Wilhelm-Klemm-Straße 10, 48149 Münster, Germany*
[b]*Institut für Festkörpertheorie, Westfälische Wilhelms-Universität Münster, Wilhelm-Klemm-Straße 10, 48149 Münster, Germany*
[c]*Hiroshima Synchrotron Radiation Center, Hiroshima University, Higashi-Hiroshima 739-0046, Japan*

Keywords: ARPES, Spin ARPES, Rhenium, Electronic Structure, Surface States, Spin-Orbit Coupling

The appearance of surface states is characteristic for semi-infinite crystals caused by the broken symmetry at the surface. Their description for understanding surface properties is a highly noticed and still ongoing research topic in various fields such as electronic surface states and surface states in photonic and phononic crystals. Theoretically, two paradigmatic concepts have been used to describe electronic surface states: Tamm and Shockley states.

The Re(0001) surface hosts both types of electronic surface states in neighboring but qualitatively different energy gaps. Spin-orbit coupling (SOC) generates a double "W"-shaped energy vs. $k_\parallel$ dispersion by mixing both types of states and lifting their spin degeneracy. We have investigated this novel and peculiar surface-state behavior by means of spin- and angle-resolved photoemission (SARPES) at BL-9B, tight-binding calculations as well as density functional theory (DFT) (including the photoemission process).

ARPES measurements of the Re(0001) surface are shown in Fig. 1. Figure 1(a) presents a constant energy contour (CEC) at $E-E_F$ = -55meV and reflects the sixfold symmetry of the hcp(0001) surface with intensity asymmetries for positive and negative k_x caused by the symmetry breaking of the incoming light. The dispersion along the ΓK and ΓM directions are shown in Figs. 1(b) and 1(c) and the second derivative of the data in Fig. 1(c) can be inspected in Fig. 1(d). Close to E_F, five bands are resolved with increasing wavevector: an almost circular band with two components of unequal intensity (α low and β high), a rather faint band γ with hexagonal warping, and a doublet of bands (δ and δ').

We performed DFT calculations including SOC for the Re(0001) surface. A "W"-shaped surface band stands out, becoming resonant with bulk states above E_F around Γ. Below E_F, the dispersion resembles that of the experimentally measured α, β, and γ bands. To reveal the origin of these surface bands, we consider DFT results neglecting SOC for two different surface potentials: The self-consistently computed surface potential (*real* surface) and a truncated surface potential (*ideal* surface). Surface states of the *real* surface that vanish at the *ideal* surface are called Tamm states. Shockley states, however, are only slightly shifted in energy (and exist in inverted band gaps only). This approach allows us to identify a Tamm-type state in the band gap around $|k_\parallel|$ < 0.48 Å^{-1} and a Shockley-type state in a band gap with $|k_\parallel|$ > 0.33 Å^{-1}.

For a qualitative understanding of the present hybridization effects, we developed a microscopic tight-binding model which comprises the Tamm and Shockley states under the influence of spin-orbit coupling. We find that the two states interact with each other leading to a double "W"-shaped state which nicely agrees with the results of the DFT calculation as well as the experimental findings.

SARPES measurements allow us to gain insight into the role of SOC on the double "W"-shaped surface state, as can be seen in Fig. 2(b). Figures 2(a) and 2(c) show DFT calculations for the intrinsic spin polarization and the expected spin polarization including final-state effects in the photoemission process, respectively. The surface states can be identified in Fig. 2(b) and have been labelled α-δ in accordance with Fig. 1. The SARPES data for θ ≈ +5° and -5° prove the expected opposite spin character of the α and β branches as well as their reversal upon a sign change in θ, which confirms the Rashba-type spin behavior as

predicted by our DFT calculations as well as the tight-binding model. While the sign of the intrinsic spin expectation value at the γ branch deviates from the SARPES results, the inclusion of final-state effects leads to good agreement.

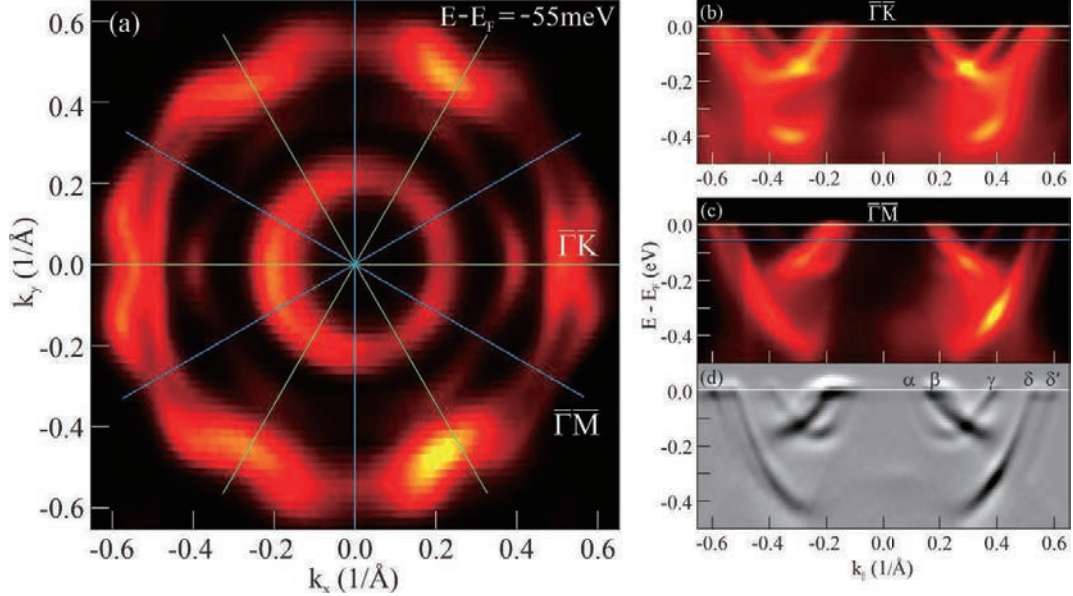This work has been published in Holtmann *et al.*, Phys. Rev. B **105**, L241412 (2022).


FIGURE 1. ARPES measurement of Re(0001) using *p*-polarized light of hν=24eV. (a) Constant energy contour (CEC) at E-E_F=-55meV. High-symmetry directions ΓK and ΓM are indicated by green and blue lines, respectively. (b,c) E($k_∥$) dispersions along ΓK and ΓM. Lines indicate the energy of the CEC in (a). (d) Second derivative of the data along ΓM in (c). The photoelectron intensity is given on a linear color scale (black-red-yellow) in (a-c). The energy resolution was <25meV and the angle resolution was <1°.

FIGURE 2. (a) DFT calculation of the Re(0001) surface along ΓM. Red (blue) dots indicate the intrinsic spin expectation value (Rashba component) for spin-up (spin-down) electrons of the surface states. (b) Experimental spin-resolved energy distribution curves (EDC) for *p*-polarized light with hν = 24eV for selected electron emission angles θ. (c) Calculations including matrix elements with free-electron-like final states to model SARPES results with hν = 24eV. The dot size is a measure of the expected spectral intensity. The approximate "paths" of the energy distribution curves within the E($k_∥$) plot are marked by green lines in (a) and (c).
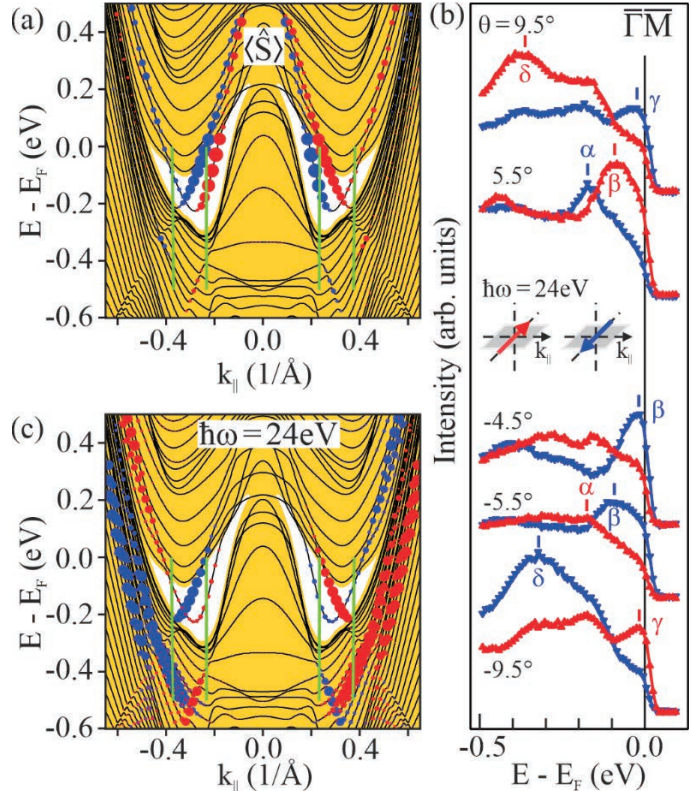
REFERENCES

1. S. Ouazi *et al.*, *Surf. Sci.* **630**, 280 (2014).
2. A. Urru and A. Dal Corso, *Surf. Sci.* **686**, 22 (2019).
3. H. J. Elmers *et al.*, *Phys. Rev. Research* **2**, 013296 (2020)
4. J. Regel *et al.*, *Phys. Rev. B* **102**, 115404 (2020)
5. S. Schemmelmann *et al.*, *Phys. Rev. B* **104**, 205425 (2021)

Spin-polarized band structures of Ga-rich Fe₃Ga film as a promising material for high thermoelectric performance

Kiyotaka Ohwada[a], Takashi Kono[b], Shogo Ushio[a], Kazuki Goto[c,d], Koji Miyamoto[e], Taichi Okuda[e], Hiroyasu Nakayama[c], Yuya Sakuraba[c] and Akio Kimura[b,f]

[a]*Department of Physics, Faculty of Science, Hiroshima University, 1-3-1 Kagamiyama, Higashi-hiroshima 739-8526, Japan*
[b]*Department of Physical Sciences, Graduate School of Science, Hiroshima University, 1-3-1 Kagamiyama, Higashi-hiroshima 739-8526, Japan*
[c]*Research Center for Magnetic and Spintronic Materials, National Institute for Materials Science, 1-2-1 Sengen, Tsukuba 305-0047, Japan*
[d]*Graduate School of Pure and Applied Sciences, University of Tsukuba, Tsukuba 305-8571, Japan*
[e]*Hiroshima Synchrotron Radiation Center, Hiroshima University, 2-313 Kagamiyama, Higashi-Hiroshima, Hiroshima 739-0046, Japan*
[f]*Physics Program, Graduate School of Advanced Science and Engineering, Hiroshima University, 1-3-1 Kagamiyama, Higashi-hiroshima 739-8526, Japan*

Thermoelectric materials are very promising for solving environmental problems because they can directly convert waste heat energy into electrical energy. They have so far been based on the so-called Seebeck effect, which generates an electric field in a direction to the heat flow. Since it is a one-dimensional phenomenon, it becomes an obstacle in minimizing the size and manufacturing cost. On the other hand, the the anomalous Nernst effect (ANE), which appears usually in ferromagnetic materials, makes it possible to apply it to complex curved surfaces due to its three dimensional nature. Therefore, the ANE has a great potential for application in energy harvesting technology.

Recently, a giant ANE up to 2.4 μV/K, which is two order of magnitude larger than that of pure Fe, has been experimentally found in the binary ferromagnetic alloy $Fe_{1-x}Ga_x$ consisting only of earth abundant and non-toxic elements [1,2]. A recent theoretical study suggests that such a remarkable ANE originates from an intrinsic mechanism caused by a peculiar band structure. To elucidate the mechanism of ANE and develop the thermoelectric device with higher performance, a direct observation of the band structures with spin resolution is essential. However, no experimental evidence on the spin resolved band structures have been missing so far.

Motivated by this, we have carried out a spin- and angle-resolved photoelectron spectroscopy (spin-ARPES) measurement on $Fe_{72}Ga_{28}$ thin film. The thin film sample was deposited on MgO(001) substrate *via* magnetron sputtering method at NIMS (Tsukuba) and transferred to the spin-ARPES apparatus (Hiroshima Univ.) using the vacuum suitcase chamber. The experiment was performed at HiSOR BL-9B using the VLEED spin detector attached to the hemispherical analyzer [3].

Figure 1(a) shows the ARPES image acquired along [110] direction with a photon energy of 60 eV. We find steeply dispersive bands that cross the Fermi level (E_F) around $k_{||} = \pm 0.5\,\text{Å}^{-1}$. No recognizable features are observed for $|k_{||}| < 0.5\,\text{Å}^{-1}$ above $E\text{-}E_F = 1.0$ eV, whereas less dispersive features with the rather strong intensity are observed at $E\text{-}E_F = -1.0 \sim -1.5$ eV. The spin-resolved energy distribution curves (EDC) at $k_{||} = 0\,\text{Å}^{-1}$ (cut 1), 0.60 Å^{-1}(cut 2), 0.79 Å^{-1}(cut 3) and 1.12 Å^{-1}(cut 4) [see panel (a)] are shown in Fig. 1(b). Minority-spin EDCs for cut 1 and 2 show a peak near $E\text{-}E_F = 0$ eV, which confirms a minority spin character for the steeply dispersive bands crossing E_F near $k_{||} = \pm 0.5\,\text{Å}^{-1}$.The minority-spin

EDC at $k_{||} = 0 \text{ Å}^{-1}$ (cut 1) shows a single peak at $E\text{-}E_F$ = -1.1 eV, while the majority-spin counterpart exhibits a broad feature at the similar energy that can be roughly decomposed into two intensity maxima at -1.0 and -1.2 eV. It tells us that the less dispersive feature shown in Fig. 1(a) near $k_{||} = 0 \text{ Å}^{-1}$ involves three distinctive bands possessing majority, minority and majority spin characteristics at $E\text{-}E_F$ = -1.0, -1.1 and -1.2 eV, respectively. All of the experimental results shown here are reasonably explained by the theoretical band structures using the first principles calculation (*not shown*) when the theoretical E_F is shifted towards the lower energy (higher binding energy) by about 100 meV. Since the predicted nodal webs, which should be responsible for the higher Nernst coefficient, are still located above E_F, the further electron doping would be necessary to maximize the transverse thermoelectric performance.
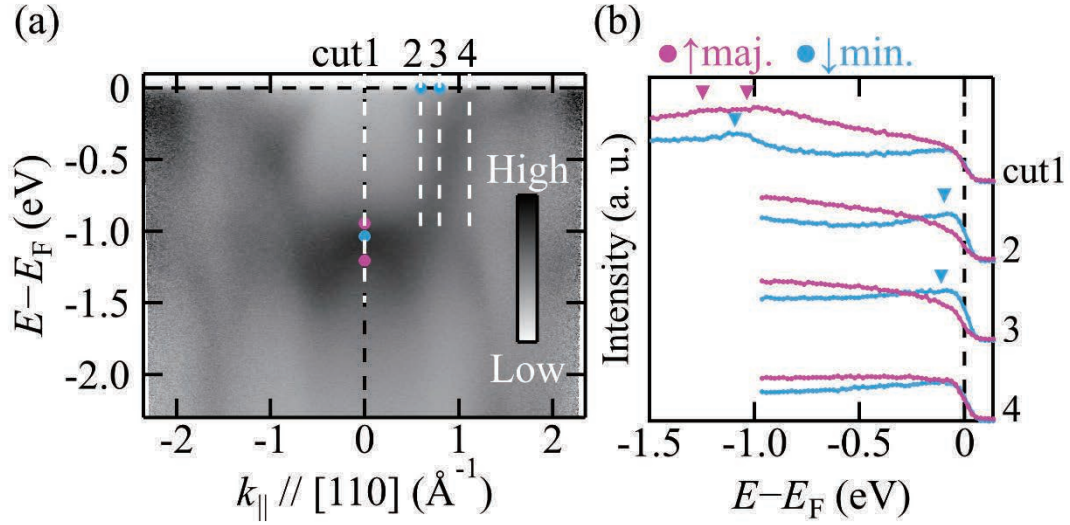

Figure 1 (a) ARPES image of $Fe_{72}Ga_{28}$ thin film along [110] direction acquired at a photon energy of 60 eV. (b) Spin-resolved EDC in majority (red) and minority (blue) spin channels at $k = 0 \text{ Å}^{-1}$ (cut 1), 0.60 Å^{-1} (cut 2), 0.79 Å^{-1} (cut 3) and 1.12 Å^{-1} (cut 4).

REFERENCES

1. H. Nakayama *et al.*, Phys. Rev. Mater. **3**, 114412 (2019).
2. A. Sakai *et al.*, *Nature* **581**, 53 (2020).
3. T. Okuda *et al., Rev. Sci. Instrum.* **82**, 103302 (2011).

Study of the Electronic Structure of the Chiral Crystal NbSi$_2$

Cheng Zhang[a], Koji Miyamoto[a], Tatsuya Shishidou[b], Ryoga Amano[c],
Taisei Sayo[c], Chiho Shimada[c], Yusuke Kousaka[c], M. Weinert[b],
Yoshihiko Togawa[c], and Taichi Okuda[a]

[a]Hiroshima synchrotron Radiation Center, Hiroshima University, 2-313 Kagamiyama, Higashi-Hiroshima 739-0046, Japan,
[b] Department of Physics, University of Wisconsin-Milwaukee, Wisconsin 53201, USA
[c] Deparment of Physics and Electronics, Graduate School of Engineering, Osaka Metropolitan University, 1-1 B4, Gakuen-cho, Naka-ku, Sakai, Osaka 599-8531, Japan

Keywords: Electronic structure, Chiral crystal, ARPES.

It is known that chirality plays an important role in the biology, such as the fact that amino acids contained in living organisms have only one chirality called L-isomer. Recently, even in the field of solid state physics, the chiral materials are attracting attention since the chiral structure causes interesting physical phenomena such as the peculiar spin texture of Te caused by its chiral structure [1]. In addition, so-called chirality induced spin selectivity effect (CISS effect), in which spin-polarized current is generated when current is passed through a material with a chiral structure has been observed in some chiral molecules [2,3].

As shown in Fig. 1, NbSi$_2$ is an inorganic material having a chiral crystal structure. Interestingly the CISS effect has been observed also in NbSi$_2$ by transport measurement, recently [4]. However, the detailed study of the electronic structure of NbSi$_2$ has not been reported so far. Thus, in this study we attempted to observe the electronic states of NbSi$_2$ by angle-resolved photoelectron spectroscopy (ARPES).

The ARPES measurement was performed at BL-9B of HiSOR. Since the NbSi$_2$ has no cleaving plane we cannot obtain the clean surface by cleaving. Therefore, as in Fig.1 (a) the NbSi$_2$ single crystals were first cut perpendicular to the c-axis. Then after mechanically polished the sample surface, the clean surfaces were obtained by the cycles of Ar ion sputtering and annealing. As the results, the sharp LEED pattern was successfully observed as in Fig. 1(b). We have measured the NbSi$_2$ crystals having different chirality(P6$_2$22 and P6$_4$22 in the space group). Figure 2 (b) and (c) show energy band structure of NbSi$_2$ with P6$_2$22 observed by ARPES along the high-symmetry lines Γ-K, Γ-M, respectively. The clear dispersions ensure the sample quality and the cleanliness of the surface. Figure 2 (a) shows calculated energy band structure by DFT along the high-symmetry lines in the Brillouin zone (see Fig. 1(e)). The calculated bands along Γ-K, Γ-M lines are overlayed on the experimental results in Fig. 2(b) and (c). As in the figure the main upward dispersion around the Γ point as well as the relatively flat bands at around E$_B$=2.0 eV are fairly reproduced by

the calculation. Note that the calculated bands are shifted about 0.2 eV for the better correspondence between the experiment and the calculation. In addition, we have also observed the constant energy contours of the bands and found the windmill like pattern which is depending on the chirality (not shown here). The reason why such a pattern is observed is currently under consideration [5].
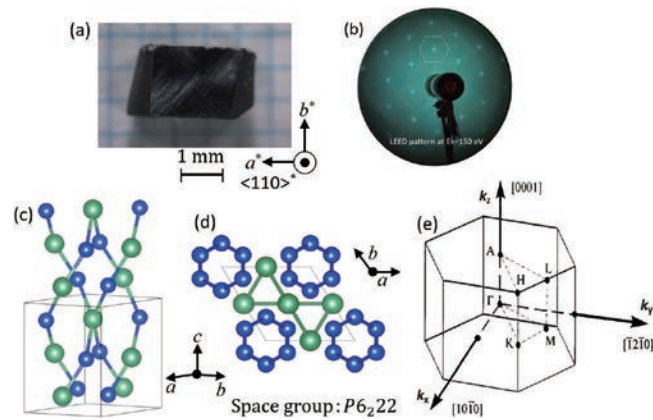

Figure 1. (a)NbSi$_2$ single crystal grown by fusion method. (b), LEED (Low-energy electron diffraction) pattern of the polished surface after annealing and argon sputtering (E$_k$=150 eV). (c), (d), Side view and top view of the crystal structure and primitive unit cell (thin lines) of the right-handed NbSi$_2$ (space group: P6$_2$22). The large (small) spheres correspond to niobium (silicon) atoms. (e), The first Brillouin zone of NbSi$_2$ and its high symmetry points.
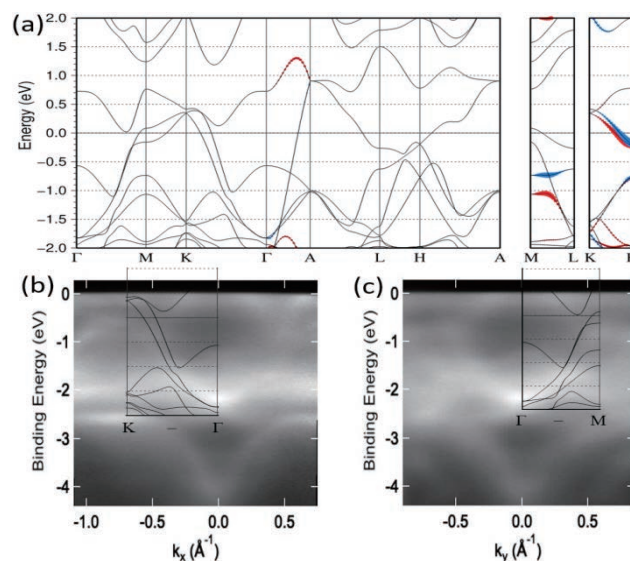

Figure 2. (a)Energy band structure calculated along the high-symmetry lines by DFT. (b)-(c) Energy band structure experimentally observed by ARPES at hν=50 eV along the high-symmetry lines Γ-K, Γ-M, respectively. The calculated band structure is also overlapped.

REFERENCES

1) M. Sakano et al., Radial spin texture in elemental tellurium with chiral crystal structure, Phys. Rev. Lett. 124, 136404 (2019).
2) R. Naaman and D. H. Waldeck, Chiral-induced spin selectivity effect, J. Phys. Chem. Lett. 3, 2178 (2012).
3) R. Naaman and D. H. Waldeck, Spintronics and chirality: Spin selectivity in electron transport through chiral molecules, Annu. Rev. Phys. Chem. 66, 263 (2015).
4) Kohei Shiota, Akito Inui et al., Chirality-Induced Spin Polarization over Macroscopic Distances in Chiral Disilicide Crystals, Phys. Rev. Lett. ,127, 126602 (2021).
5) C. Zhang et al. in preparation.

Spin-Resolved Resonant Photoelectron Spectroscopy For Co₂MnSi Heusler Alloy film

Kazuki Sumida[a], Yukiharu Tekeda[a], Kiyotaka Ohwada[b], Karen Nakanishi[b], Koji Miyamoto[c], Taichi Okuda[c], Akio Kimura[b], and Yuya Sakuraba[d]

[a]Materials Sciences Research Center, Japan Atomic Energy Agency, Hyogo 679-5148, Japan
[b]Graduate School of Advanced Sciences and Engineering,
Hiroshima University, Higashi-Hiroshima 739-8526, Japan
[c]Hiroshima Synchrotron Radiation Center, Hiroshima University,
2-313 Kagamiyama, Higashi-Hiroshima 739-0046, Japan
[d]Research Center for Magnetic and Spintronic Materials, National Institute for Materials Science,
Sengen 1-2-1, Tsukuba 305-0047, Japan

Keywords: Spin-resolved photoelectron spectroscopy, Resonant photoelectron spectroscopy, Heusler alloy, Half-metal.

Many Co-based Heusler alloys are known to show high spin-polarization and Curie temperature. Among them, Co₂MnSi is theoretically predicted to be a half-metallic ferromagnet exhibiting 100% spin-polarization at the Fermi energy (E_F) due to its insulating (metallic) feature at the minority-spin (majority-spin) state. In fact, a huge output exceeding 2000% has been reported for tunnel magnetoresistance (TMR) devices using Co₂MnSi films as ferromagnetic electrodes. However, such a giant TMR ratio is observed only at low temperatures, and the output drastically decreases to ~200% at room temperature [1]. Theory tells us that the thermal instability of magnetic moments at the surface of Co₂MnSi or at the interface between Co₂MnSi and insulators, such as MgO, is responsible for the drastic temperature dependence of the TMR ratio [2]. Nevertheless, the spin-polarized electronic structure at the surface or interface of Co₂MnSi films is rarely investigated by experiments, so far.

In this work, we performed surface-sensitive spin-resolved resonant photoelectron spectroscopy (SR-PES) to investigate the spin-polarized surface electronic structure of Co₂MnSi thin film. Epitaxial Co₂MnSi thin film was deposited on a MgO substrate with Cr and Ag buffer layers using rf magnetron sputtering at room temperature. To obtain $L2_1$-ordered structure, the fabricated sample was annealed at 550°C for 30 min. Subsequently, the sample was transferred from the sputtering chamber at National Institute for Materials Science to the BL-9B at HiSOR using a portable suitcase chamber. Prior to the SR-PES measurements, the sample was annealed again at 550°C for 30 min, and a magnetic field as large as ~0.1 T was applied to the sample along the [110] direction using a permanent magnet at room temperature. The energy resolution for PES (SR-PES) was set to 40 meV (45 meV). The effective Sherman function was 0.3 for the spin-resolved measurements. During the SR-PES measurements, the temperature was maintained at 30 K. We have also carried out the first-principles calculations for Co₂MnSi using WIEN2k program [3]. The exchange-correlation energy was treated using the generalized gradient approximation [4].
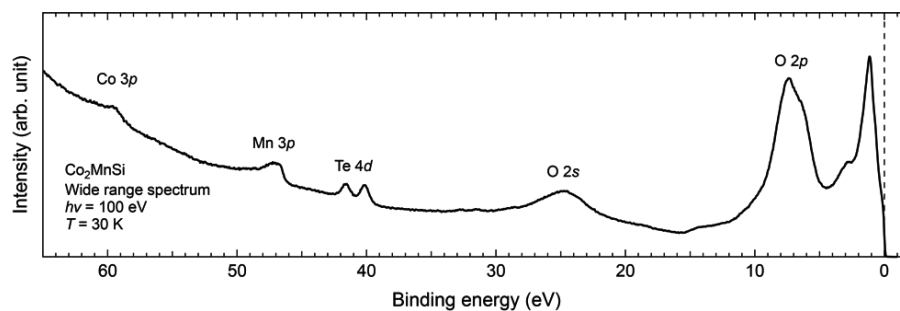

FIGURE 1. Wide energy range photoelectron spectrum recorded at hv = 100 eV.

Figure 1 shows the wide energy range photoelectron spectrum recorded at $hv = 100$ eV. Although we confirmed the Co and Mn $3p$ core levels, additional peak structures stemming from O and Te were observed. Such contaminations were probably caused during the sample transfer and could not be removed by the annealing. This means that the Co_2MnSi surface reacts rapidly with molecular oxygen or other chalcogenides even in vacuum conditions.

To explore the effect of the contamination on the electronic structure, we next performed resonant PES. Figure 2(a) shows the incident photon energy dependent valence band spectra recorded at 48 to 54 eV, which covers Mn $3p$-$3d$ resonance [5]. One can see that the photoelectron intensity suddenly decreased at 49.5 eV (light blue color) but increased again above 50 eV. To emphasize this variation, we plot the constant initial state (CIS) spectra at $E_B = 1.1$ and 3.2 eV in Fig. 2(b). For both CIS spectra, we found the so-called "Fano line" profiles indicating the Mn $3p$-$3d$ resonance. Figure 2(c) shows the difference spectrum obtained by subtracting the on-resonant (51.0 eV) and off-resonant spectra (49.5 eV). The experimentally verified Mn $3d$ resonant spectrum is qualitatively reproduced by the calculated partial density of state (PDOS) of Mn $3d$ orbital of the pristine Co_2MnSi [lower panel of Fig. 2(c)].

To get a deeper insight into the surface electronic structure, we performed the spin-resolved measurement. Figures 2(d,e) show the spin-resolved valence band spectra and spin-polarization at Mn $3p$-$3d$ resonant condition (51.0 eV). We found the positive spin-polarization around $E_B = 0.0 - 1.0$ eV and $2.0 - 3.5$ eV while the negative spin-polarization can be seen around $E_B = 1.6$ eV (see green arrow). Such sign reversal features were well-reproduced by our calculations for Mn $3d$ PDOS shown in Figs. 2(f,g). However, the magnitude of the experimentally obtained spin-polarization is about one-twentieth smaller than that of the theoretical value. This remarkable difference might be caused by the spin scatterings at the surface contamination layers during the photoemission process. These results, therefore, tell us that it is important to prevent surface contamination to achieve higher spin-polarization.
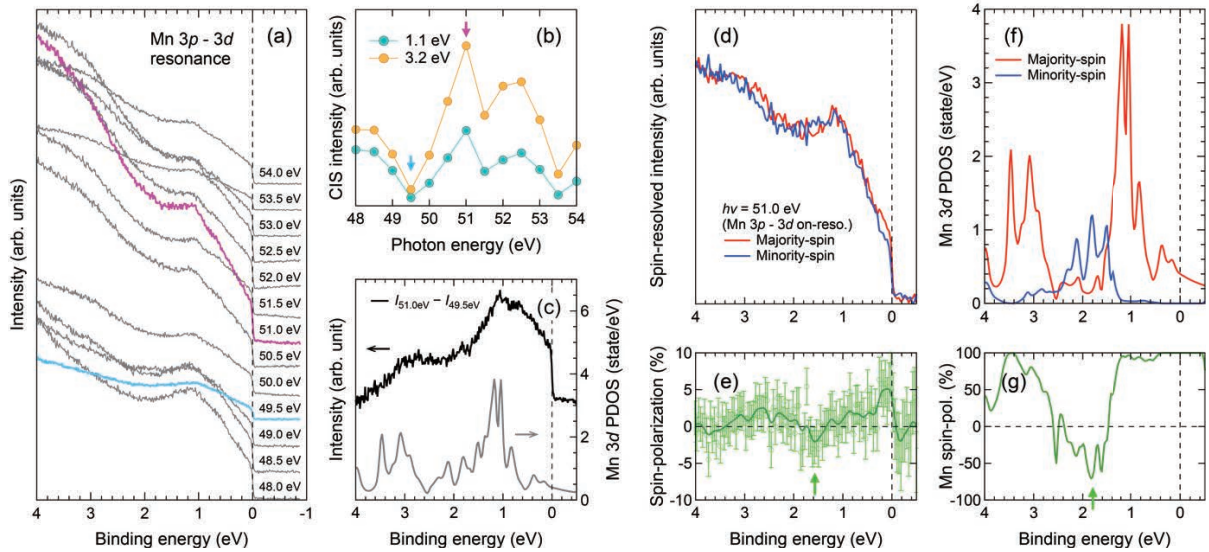

FIGURE 2. (a) Incident photon energy dependent spin-integrated valence band spectra recorded at 48 – 54 eV. The photoelectron intensities are normalized by the mirror current. (b) CIS spectra at $E_B = 1.1$ and 3.2 eV. Magenta and light blue arrows represent photon energies used for the on- and off-resonances. (c) Difference spectrum between the on- and off-resonances and calculated Mn $3d$ PDOS. The background signals are subtracted by the Shirley method. (d,e) Spin-resolved valence band spectra and spin-polarization recorded at $hv = 51$ eV. The green arrow indicates the negative spin-polarization. (f) Calculated spin-resolved PDOS for Mn $3d$ states. (g) Calculated Mn spin-polarization evaluated from the difference between Mn $3d$ majority-spin and minority-spin PDOSs.

REFERENCES

1. S. Tsunegi *et al.*, *Appl. Phys. Lett.* **93**, 112506 (2008).
2. A. Sakuma, Y. Toga, and H. Tsuchiura, *J. Appl. Phys.* **105**, 07C910 (2009).
3. P. Blaha *et al.*, *J. Chem. Phys.* **152**, 074101 (2020).
4. J. P. Perdew, K. Burke, and M. Ernzerhof, *Phys. Rev. Lett.* **77**, 3865 (1996).
5. S. Huefner and G. K. Wertheim, *Phys. Lett. A* **47**, 349 (1974).

Spin-resolved ARPES study of the electronic structure in antiferromagnet without inversion symmetry

T. Iwata[a], K. Nakanishi[a], A. Kimura[a], K. Miyamoto[b], T. Okuda[b],
H. Takatsu[c] and K. Kuroda[a]

[a]Graduate School of Advanced Science and Engineering, Hiroshima University, 1-3-1 Kagamiyama,
Higashi-Hiroshima 739-8526, Japan
[b]Hiroshima Synchrotron Radiation Center, Hiroshima University, 2-313 Kagamiyama, Higashi-Hiroshima
739-0046, Japan
[c]Deperment of Physics, Graduate School of Science, Kyoto University, Kyoto 606-8502, Japan

Antisymmetric spin-orbit coupling (SOC) in noncentrosymmetric materials has drawn considerable attention, since it is thought to be able to apply spintronics devices. For instance, Rashba effect leads to the spin splitting by the strong SOC in collaboration with symmetry breaking. In recent years, S. Hayami *et al.* proposed that a giant Rashba-like spin splitting band structure is driven by magnetic phase transition without spin-orbit coupling in the antiferromagnet [1]. $PdCrO_2$ with alternating layers of Pd and CrO_2 layers was finally predicted to be a candidate to exhibit the novel spin splitting. In this compound, the localized spin moment of Cr^{3+} shows a 120° antiferromagnetic structure below the Néel temperature (37. 5 K). Up to now, significant interplay between the conduction electrons and the localized spins has been suggested, and however there is no experimental report regarding the possible spin splitting.

In this work, we studied the electronic band and spin splitting of $PdCrO_2$ by using spin-resolved ARPES at BL-9B of HiSOR. Figure 1(a) presents a repetitive ARPES image along high symmetry momentum line, which clearly shows two-split-bands similar to the spin-splitting. To justify this, we performed spin-resolved ARPES. The results are shown in Figure 1(b-e). However, no consideration spin polarization was observed for Sx, Sy, and Sz. Thus, the split bands may originate from other origin, and their spin polarization are small.
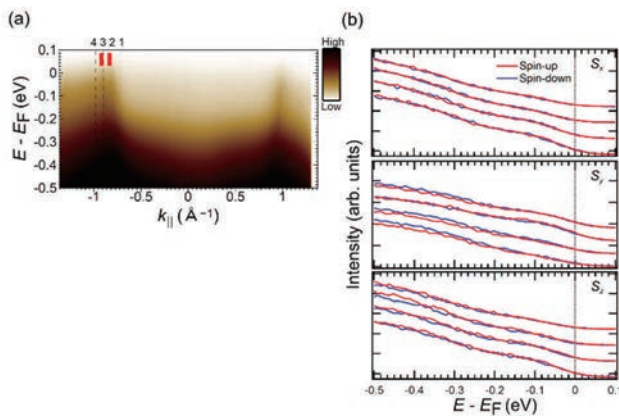

FIGURE 1. (a) ARPES band image along the Γ - K direction ($h\nu$=80 eV, T=30 K). Red markers in Fig. 1 (b) indicated the location of two bands which look like splitting. SARPES EDCs for Sx, Sy, and Sz, respectively.

REFERENCES

1. S. Hayami, Y. Yanagi, and H. Kusunose *Phys. Rev. B.* **101**, 220403, 2020.
2. H. Takatsu, H. Yoshizawa, S. Yonezawa, and Y. Maeno. *Phys., Rev., B.* **79**. 104424. 2009.
3. H. Takatsu, S. Yonezawa, S. Fujimori, and Y. Maeno. *Phys., Rev., Letters.* **105**. 137201. 2010.

Minority-spin Dominated Band Structure Near the Fermi Energy of Fe₄N Film Revealed by Spin- And Angle-Resolved Photoemission Spectroscopy

Karen Nakanishi[a], Kiyotaka Ohwada[b], Kenta Kuroda[b], Kazuki Sumida[c], Koji Miyamoto[d], Taichi Okuda[d], Shinji Isogami[e], Keisuke Masuda[e], Yuya Sakuraba[e], Akio Kimura[a,b]

[a]*Department of Physics, Faculty of Science, Hiroshima University, Higashi-Hiroshima 739-8526, Japan*
[b]*Graduate School of Advanced Science and Engineering, Hiroshima University, 1-3-1 Kagamiyama, Higashi-hiroshima 739-8526, Japan*
[c]*Materials Sciences Research Center, Japan Atomic Energy Agency, Hyogo 679-5148, Japan*
[d]*Hiroshima Synchrotron Radiation Center, Hiroshima University, 2-313 Kagamiyama, Higashi-Hiroshima 739-0046, Japan*
[e]*National Institute for Materials Science, 1-2-1 Sengen, Tsukuba 305-0047, Japan*

Fe₄N has attracted a great deal of attention as a strong candidate for spintronic materials because of the inverse tunneling magnetoresistance (TMR) effect [1], the negative anisotropic magnetoresistance [2], and an enhanced spin-pumping efficiency [3,4]. An almost 100% negative spin polarization in the conductivity has been predicted for Fe₄N, where the hybridization between Fe 4sp and N 2sp orbitals plays an important role [5], while the spin polarization in the density of states at the Fermi level (E_F) is as small as -0.6. The spin polarization for Fe₄N film was measured by the point-contact Andreev reflection experiment, while its sign remained undetermined [6]. The TMR was often used to estimate the spin-polarization using Jullier's model [7], which was significantly influenced by the film-substrate interface. It is reminded that the unexpectedly high magnetoresistance at room temperature was reported for Fe/MgO/Fe magnetic tunneling junction, where the band-selective electron conductivity takes place in 'non-half-metallic' ferromagnetic layers [8]. It tells us that an experimental determination of spin- and wavenumber-dependent band structures are quite important.

Spin- and angle-resolved photoemission spectroscopy (spin-ARPES) is one of the most powerful experimental tools to clarify the spin-dependent electronic band structures. It requires a single crystal with remanent magnetization. In fact, there have been no direct experimental observations of the electronic band structures for the bulk Fe₄N due to the lack of cleavage plane and the non-saturating magnetization in the absence of an external magnetic field. The previous spin- resolved photoemission study on the Fe₄N film reported the negative spin polarization near E_F. However, the ion-sputtering of *ex-situ* grown film caused the deficiency of N atoms and the measured spin polarization remained inaccurate [9].
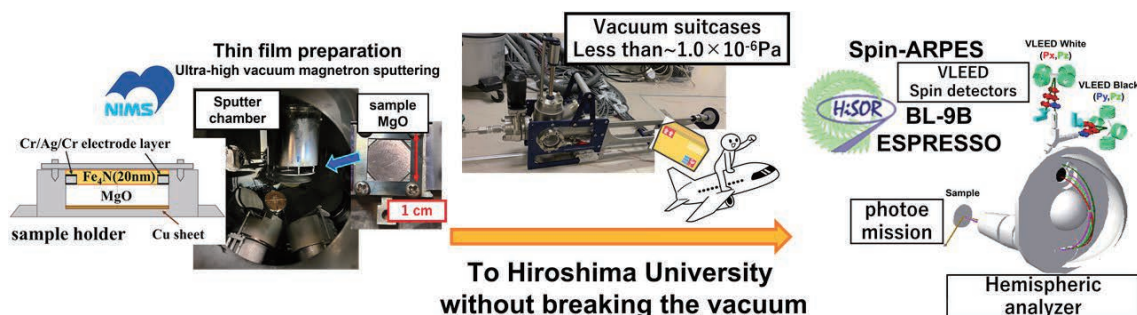

FIGURE 1. Growth of Fe₄N thin film and in-vacuum transportation to HiSOR.

To overcome this problem, we have grown the Fe_4N thin film and *in situ* performed spin-ARPES. The thin film samples were grown on MgO substrates by an ultrahigh-vacuum magnetron sputtering method at the National Institute for Materials Science (NIMS). The degree of order for nitrogen atoms in the film was evaluated to be 0.95 by the in-plane X-ray diffraction. An electrode layer of Cr/Ag/Cr was inserted to increase the electrical conductivity between the thin film and the sample holder, being indispensable for the spin-ARPES measurement.

The film samples were transported from NIMS to the preparation chamber of the spin-ARPES apparatus at HiSOR *via* the vacuum suitcase chamber. The thin films were reheated to 390~400°C to remove the contaminants adsorbed during the transportation. No nitrogen deficiency and no other impurities were detected by the Auger electron spectroscopy and the flat (001) surface was ensured by the sharp LEED spots. Spin-ARPES measurement was performed utilizing the ESPRESSO machine composed of the hemispherical analyzer and the VLEED-type spin detector with *s*- and *p*- polarized undulator radiation at BL-9B of HiSOR [7]. The photoelectron spin polarization (P) was estimated from the measured intensity asymmetry $A = (I^+ - I^-)/(I^+ + I^-)$ with the effective Sherman function ($S_{eff} = 0.3$) through the relation $P = A/S_{eff}$, where $I^+(I^-)$ represents the reflected electron intensity at the positively (negatively) magnetized Fe(001)-p(1×1)O target of the spin detector.

Figure 2(a) shows the ARPES image of Fe_4N thin film in the ΓM direction of the bulk Brillouin zone (Fig.2(c)). We have observed three band structures that cross E_F at $k_\parallel$ = -1.0, -0.5 and +0.5 Å^{-1}. Figure 2(b) shows the spin-resolved energy distribution curves deduced by $I_{\uparrow\downarrow} = 0.5I(1 \pm P)$ at the fixed wavenumber of the red line in Fig.2(a), where $I_\uparrow$ ($I_\downarrow$) corresponds to the photoelectron intensity in the majority (minority) spin channel and $I = I_\uparrow + I_\downarrow$. We find that $I_\uparrow$ is dominant in the energy (E-E_F) from -1.6 eV to -0.5 eV, while $I_\downarrow$ gradually increases with increasing energy and get much higher than $I_\uparrow$ in the vicinity of E_F.

In summary, the minority-spin dominated character of the band structures in the vicinity of E_F has been unveiled experimentally for Fe_4N thin film. Our finding provides deep insights into the mechanism of the inverse tunneling magnetoresistance effect, the negative anisotropic magnetoresistance, and the enhanced spin pumping in Fe_4N, which will help the development of spintronics devices.
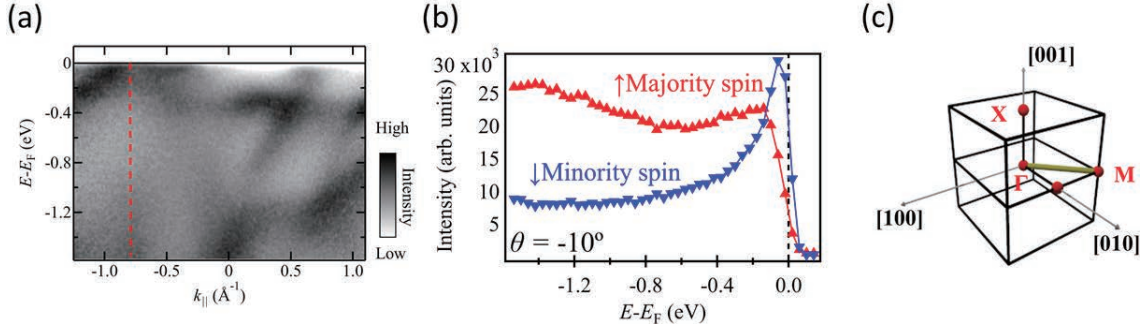

FIGURE 2. (a) ARPES energy dispersions curves along the ΓM line. (b) Spin-resolved energy distribution curves acquired at a wavenumber position denoted with red dashed line in panel (a). (c)Bulk Brillouin zone of Fe_4N.

REFERENCES

1. K. Sunaga, M. Tsunoda, and K. Komagaki *et al*, J. Appl. Phys. **102**, 013917 (2007).
2. M. Tsunoda, Y. Komasaki, S. Kokado, S. Isogami, C.-C. Chen, and M. Takahashi, Appl. Phys. Express **2**, 083001 (2009).
3. S. Isogami, M. Tsunoda, M. Oogane, A. Sakuma, and M. Takahasi, Appl. Phys. Exp. **6**, 063004 (2013).
4. S. Isogami, and M. Tsunoda, Jpn. J. Appl. Phys. **55**, 043001 (2016).
5. S. Kokado, N. Fujima, K. Harigaya, H. Shimizu, and A. Sakuma, Phys. Rev. B.**73**,172410 (2006).
6. A. Narahara, K. Ito, T. Suemasu, Y. K. Takahashi, A. Rajanikanth, and K. Hono, Appl. Phys. Lett. **94**, 202502 (2009).
7. M. Julliere, Phys. Lett. **54A**, 225 (1975).
8. S. Yuasa, T. Nagahama, A. Fukushima, Y. Suzuki, and K. Ando, Nat. Mater. **3**, 868 (2004).
9. K. Ito, K. Okamoto, K. Harada, T. Sanai, K. Toko, S. Ueda, Y. Imai, T. Okuda, K. Miyamoto, A. Kimura, and T. Suemasu, J. Appl. Phys. **112**, 013911 (2012).
10. T. Okuda *et al*, Rev. Sci. Instrum. **82**, 103302 (2011).

The Ca -K edge synchrotron X-ray absorption near-edge structure of cement-treated clays mixed with limestone or granite powder

Joyce Nakayenga[a], Toshiro Hata[a] and Shinjiro Hayakawa[b]

[a] *Department of Civil and Environmental Engineering, Graduate School of Advanced Science and Engineering, Hiroshima University, Kagamiyama, Higashi-Hiroshima, Hiroshima, 739-8527, Japan*
[b] *Department of Applied Chemistry, Graduate School of Advanced Science and Engineering, Hiroshima University, Kagamiyama, Higashi-Hiroshima, Hiroshima, 739-8527, Japan*

Keywords: Cement-treated clay, limestone, granite powder, XANES
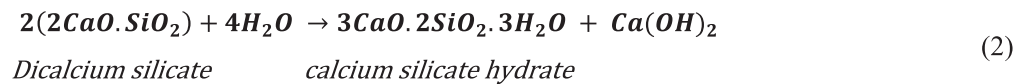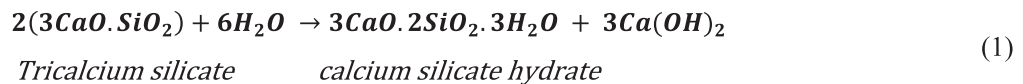
Introduction

Wasted rock powders such as granite powder and limestone have been found to enhance hydration of cement [1]. Enhanced cement hydration increases the early unconfined compressive strength (after 1 and 3 days of curing) of cement based composites which had been manifested in geomaterials referred to as cement-treated clay-granite composites [2]. The structure of cement-treated clay-granite composites is yet to be explored.

In this study, the 1- and 3-day Synchrotron X-ray absorption near-edge structure (XANES) of cement-treated clay-limestone, cement-treated clay-granite composites and cement-treated clay (control sample) were studied. The XANES structure was studied using cement hydration products calcium hydroxide and calcium carbonate.

Chemical mechanisms of cement hydration

Ordinary Portland cement contains tricalcium silicate and dicalcium silicate that upon hydration form calcium silicate hydrate and calcium hydroxide $(Ca(OH)_2)$ according to equations 1 and 2, respectively. Exposure of $Ca(OH)_2$ to air leads to the formation of calcium carbonate ($CaCO_3$) as shown in equation 3.

$$2(3CaO.SiO_2) + 6H_2O \rightarrow 3CaO.2SiO_2.3H_2O + 3Ca(OH)_2$$

Tricalcium silicate   calcium silicate hydrate   (1)

$$2(2CaO.SiO_2) + 4H_2O \rightarrow 3CaO.2SiO_2.3H_2O + Ca(OH)_2$$

Dicalcium silicate   calcium silicate hydrate   (2)

$$Ca(OH)_2 + CO_2 \rightarrow CaCO_3 + H_2O$$ (3)

Materials and Methods

Materials

Limestone or granite was mixed with cement and refrigerated distilled water for 10 minutes to form the composites without clay. The resultant composites without clay were then mixed with refrigerated Tokuyama for 30 minutes. A control sample containing clay, cement and water was also prepared for reference purposes. These composites whose composition is shown in Table 1 were cured under water at 20^0C for 1 and 3 days.

TABLE 1. Sample composition

Sample name	Cement content (%)	Clay content (%)	Rock powder content (%)	Description
Limestone	0	0	100	Raw material
Cement-treated limestone	15	0	85	
LS(850-<1μm)	15	70	30	Cement-treated clay-limestone
Granite	0	0	100	Raw material
Cement-treated granite	15	0	85	
GP(106-<1 μm)	15	70	30	Cement-treated clay-granite
Tokuyama Clay	0	0	100	Raw material
Control	15	0	85	Cement-treated clay
Calcium hydroxide	-	-	-	Reference for Ca(OH)$_2$
Calcite	-	-	-	Reference for CaCO$_3$
Aragonite	-	-	-	Reference for CaCO$_3$

Synchrotron X-ray absorption near-edge structure spectroscopy (XANES)

After the 1 and 3-day of curing, 5 mm cubes were cut from the core of cement-treated samples and microwaved to stop further chemical reactions. The cubes and raw materials (Tokuyama clay, limestone, granite and cement) were pulverized to a size of <75μm and subjected to XANES using the Ca K-edge absorption spectra [3], [4] at beamline BL-11 of the Hiroshima Synchrotron Radiation Center (HiSOR), Hiroshima University, Higashi-Hiroshima, Japan. The incident Xray energy was not calibrated. We focused on the 2 cement hydration products i.e., calcium hydroxide and calcium carbonate, where calcite, aragonite, and pure calcium hydroxide were used as reference materials.

Results

XANES of reference materials
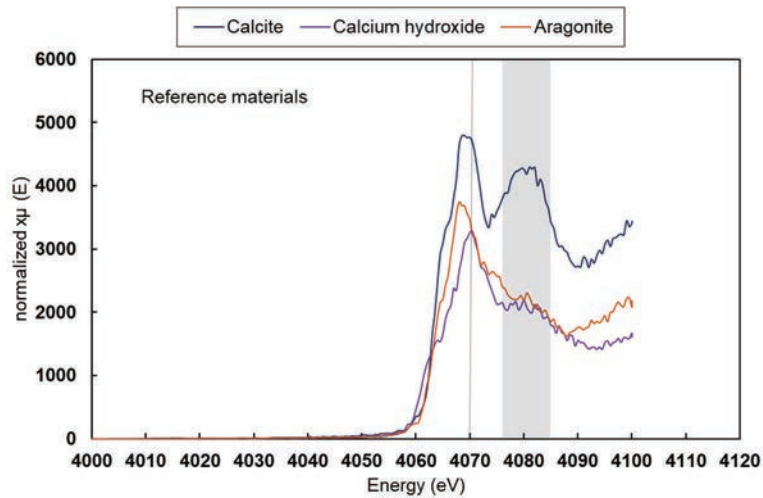
FIGURE 1. XANES spectra of reference materials: calcite, calcium hydroxide and aragonite

As shown Figure 1, the reference materials had 2 dominant peaks and the energy ranges at which they occur is shown in table 2.

TABLE 2. Dominate peaks of the reference materials

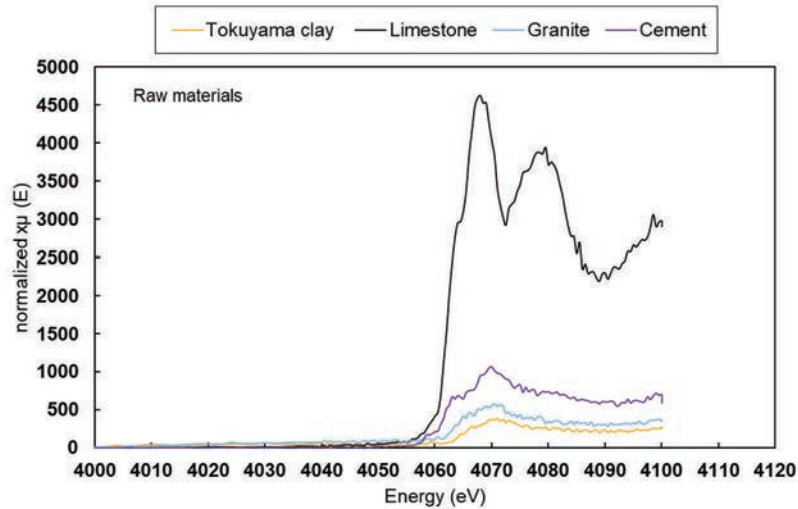| Reference	Peak 1 (eV)	Peak 2 (eV)
Calcite	4069-4070	4075-4085
Calcium hydroxide	4069-4072	4075-4085
Aragonite	4068.5-4069.5	4078-4085

FIGURE 2. XANES of raw materials: Tokuyama clay, limestone, granite, cement

As shown in Figure 2, limestone takes up the structure of calcite. Since Tokuyama clay and granite, are predominantly made of silica, the intensity of their peaks was low.

In Figure 3, the shapes of hydrated cement and cement treated granite evolve from a calcite likes structure at 1 day of curing to the calcium hydroxide like structure at 3 days. Cement treated limestone takes up the structure of calcite.
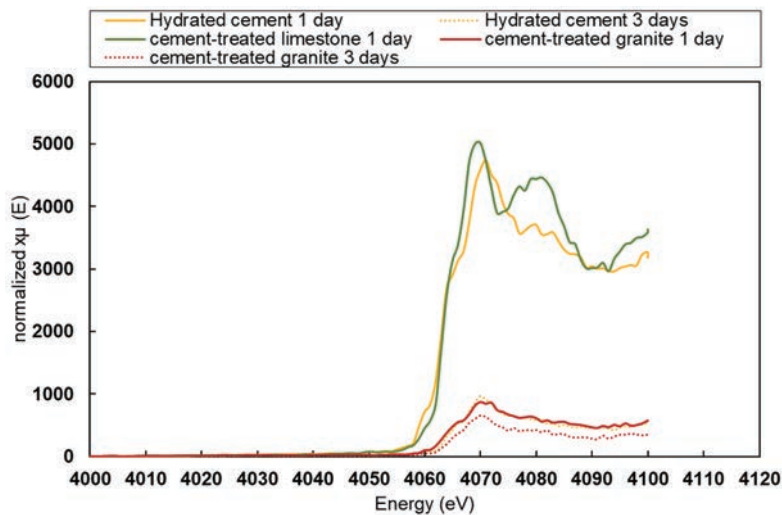

FIGURE 3. XANES of hydrated cement, cement treated limestone and cement treated granite at 1 and 3 days of curing

XANES of cement treated clay composites

The spectra of cases LS(850-<1μm), GP(106-<1 μm), and control sample are presented in Figure 4. The samples displayed 2 prominent Ca^{2+} absorption peaks at 4070 eV and between 4075 and 4085 eV. However, the peak intensity between 4076 and 4084 eV varied with the increase in curing time of the samples. This peak was almost nonexistent in case GP(106-<1 μm) at all the curing times and disappears in the control sample at 3 days of curing. The peak was persistent in case LS(850-<1μm) at all curing times. When compared to calcite, aragonite and calcium hydroxide (Figure1), at 1 and 3 days, case LS(850-<1μm) took up the shape of calcite, while case GP(106-<1 μm) took up that of calcium hydroxide. The control sample, however, took up the shape of calcite and calcium hydroxide at 1 and 3 days, respectively. In all cement-treated clay composites at 1 day, the spectra at 4076 had 1 peak just like calcium hydroxide, while at 3 days it had 2 peaks just like calcite.
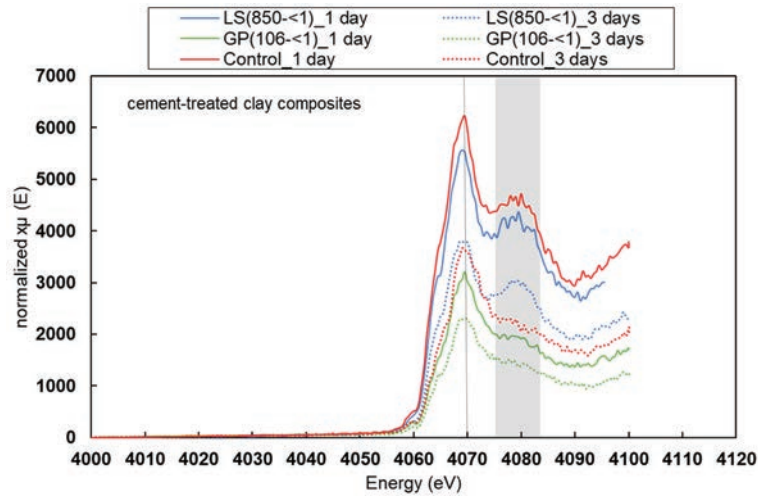
FIGURE 4. XANES spectra of cement-treated clay composites

REFERENCES

[1] D. P. Bentz, C. F. Ferraris, S. Z. Jones, D. Lootens, and F. Zunino, "Limestone and silica powder replacements for cement: early-age performance," *Cem. Concr. Compos.*, vol. 78, pp. 43–56, 2017, doi: 10.1016/j.cemconcomp.2017.01.001.

[2] J. Nakayenga, A. A. Cikmit, T. Tsuchida, and T. Hata, "Influence of stone powder content and particle size on the strength of cement-treated clay," *Constr. Build. Mater.*, vol. 305, no. February, p. 124710, 2021, doi: 10.1016/j.conbuildmat.2021.124710.

[3] S. Grangeon, F. Claret, C. Roosz, T. Sato, S. Gaboreau, and Y. Linard, "Structure of nanocrystalline calcium silicate hydrates: Insights from X-ray diffraction, synchrotron X-ray absorption and nuclear magnetic resonance," *J. Appl. Crystallogr.*, vol. 49, pp. 771–783, 2016, doi: 10.1107/S1600576716003885.

[4] J. Li *et al.*, "The chemistry and structure of calcium (alumino) silicate hydrate : A study by XANES , ptychographic imaging , and wide- and small-angle scattering," *Cem. Concr. Res.*, vol. 115, no. September 2018, pp. 367–378, 2019, doi: 10.1016/j.cemconres.2018.09.008.

Development Of A New Device For Angular Dependent Conversion Electron Yield XAFS Measurements

Shinjiro Hayakawa [a], Haruka Yoshimoto[a], Jens R. Stellhorn[a], Kenji Komaguchi[a]

a *Applied Chemistry program, Graduate School of Applied Science and Engineering,, Hiroshima University, Higashi-Hiroshima, Hiroshima 739-8527, Japan*

Introduction

X-ray absorption fine structure (XAFS) measurements in the soft X-ray region are widely conducted with X-ray fluorescence yield (XFY) method and electron yield method owing to the difficulties in preparing samples of appropriate optical thickness for the transmission method. We have been employing conversion electron yield (CEY) method [1] that utilizes the ionization of surrounding gas molecules by the energetic Auger electrons from a sample. CEY is advantageous in the sense of S/N compared to XFY owing to the extremely small fluorescence yield in the soft X-ray region. However, the use of an electrode that prevents created electron-ion pairs from the recombination has made the angular dependent measurements difficult. We have developed a new device that can make the angular dependent XAFS measurements using CEY method. The device was applied to the fractional determination of orientations in polythiophene thin films.

2. Experimental

2.1 CEY device

Principles of the CEY measurements are similar to those of X-ray detection with an ionization chamber except for the ionization source of gas molecules. Typically He gas is employed to reduce the direct ionization with X-rays, and a planer electrode has been adopted in BL-11 to avoided the recombination of the created electron-ion pair. To overcome the interference of the electrode with incident X-rays, we have adapted a rod-shaped electrode that is similar to the proportional counter (PC) for X-ray detection, and the PC could be utilized for measuring CEY from the sample placed in the counter when operated with the mixture of He and methane [2].

Figs.1 show schematic side view and the photograph of the new device. Two electrodes of semicircle rod shape were arranged below and above the beam height. The diameter of the electrode, *b*, was 6 mm, and the
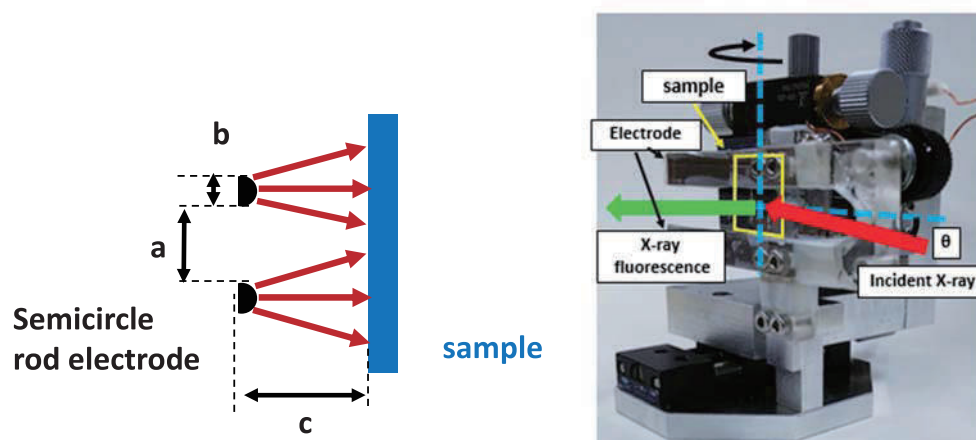
FIGURES 1. Schematic side view around the electrodes and the photograph of the new device

size was determined to make the strength of the electric field around the sample relatively uniform within the region of the ionization chamber while the electron cascade around the electrode was prevented. The clearance between the electrodes, *a*, was 8 mm, and the distance between the sample surface and the center of the electrode, *c*, was 8 mm. A sample was mounted on the rotational stage or a rotational axis of a motor for in plane rotation.

2.2 P3HT samples

Several types of poly (3-hexylthiophene-2,5-diyl) (P3HT) were spin coated onto Si or ITO glass substrates. Among them a special P3HT sample was prepared with a commercial P3HT reagent, and the surface of the ITO substrate was previously brushed with a velvet fabric. The sample showed uniaxial edge-on orientation, and the majority of the backbone of P3HT molecules were aligned along the brushing direction [3].

XAFS measurements were performed on BL-11, and both XFY and CEY were measured simultaneously. The developed new device was utilized for the XAFS measurements with the various glancing and azimuthal angles.

3. Results and discussion

Fig. 2 shows a series of sulfur K-edge XAFS spectra from the uniaxial edge-on sample. The glancing angle was 80 deg, and the incident beam was almost normal to the surface. It was clear that the XAFS spectra have azimuthal angular dependence, and the uniaxial character of the film could be explained with the angular dependences of σ^* and π^* peaks in the spectra.

Figs. 3 and 4 show azimuthal angular dependence of σ^* and π^* peak intensities. Fitting procedures with the theoretical model provided fractions of orientations in the sample.

In this presentation the principles and the advantages of the new device will be explained、and the results of the fractional determination of the P3HT orientations will be presented.
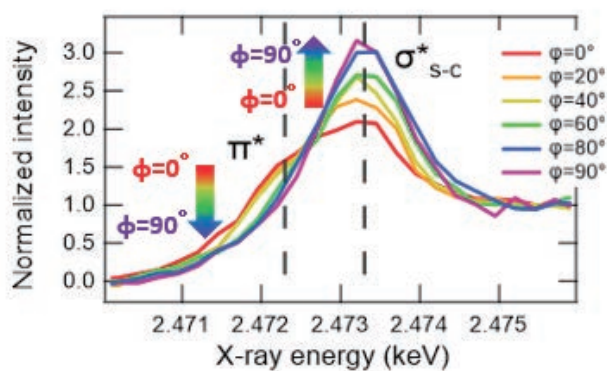

FIGURE 2. Polarization (azimuthal angle) dependence of Sulfur K-edge XAFS spectra of a P3HT film of uni-axial edge-on orientation.
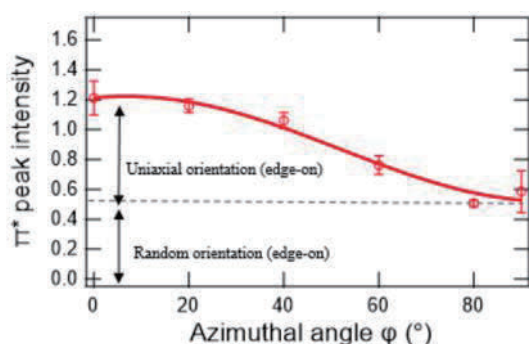

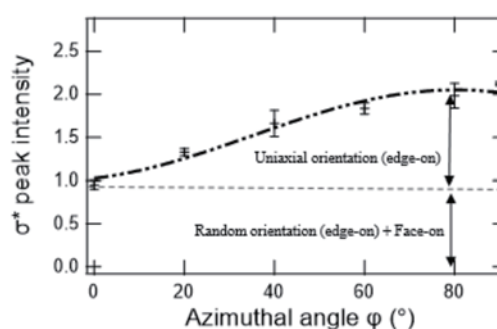**Figure 3.** Azimuthal angle dependence of π^* peak intensities

Figure 4. Azimuthal angle dependence of σ^* peak intensities

REFERENCES

1. S. Hayakawa et al., Spectrochim. Acta. B , 54B (1999) 235-240.
2. S. Hayakawa et al., Jpn. J. Appl. Phys.,38 (1999) 2161-2163.
3. M Imanishi et al., Sci.Rep.,7(2017)514,

Structure of a Novel Amorphous Organic-Inorganic Hybrid Tin Cluster Exhibiting Nonlinear Optical Effects by Low-Energy XAFS Measurements

Jens R. Stellhorn[a], Shinjiro Hayakawa[a], Benedict Paulus[b], Benjamin D. Klee[b], Wolf-Christian Pilgrim[b], Stefanie Dehnen[b]

[a] Department of Applied Chemistry, Graduate School of Advanced Science and Engineering,
Hiroshima University, Higashi-Hiroshima, Hiroshima 739-8527, Japan
[b] Department of Chemistry, Philipps University of Marburg, Marburg 35032, Germany

Keywords: non-linear optical properties, white-light generation, amorphous compound, local structure, EXAFS.

Tailored light sources have greatly advanced technological and scientific progress by optimizing colour and brilliance, improving energy efficiencies or the quantum properties of light. So called supercontinuum generators are premier examples for media with nonlinear optical (NLO) effects – far superior in some respects to other sources such as phosphorescent white light-emitting diodes (LEDs). However, unlike LEDs, most of these advanced light sources are only used for scientific purposes, as they require extreme electric field strengths which are commonly realized by high-power pulsed lasers. In contrast, the materials of interest for this research project represent a new generation of supercontinuum emitters that are readily obtained from ubiquitous resources in a simple synthesis.

In our study [1], we investigated the local structure of 4 different amorphous organotin sulfide $[(R-Sn)_4S_6]$ compounds by X-ray absorption spectroscopy. These compounds exhibit a non-linear optical response upon irradiation with a continuous-wave near-infrared laser.[2-4] Their basic structural motif is a hetero-adamantane cluster with different organic substituents R. The nature of the NLO response depends strongly on the morphology of the material, which is influenced by the choice of the organic substituents, leading to either a second harmonic generation or the generation of a supercontinuum, potentially appearing as white light.
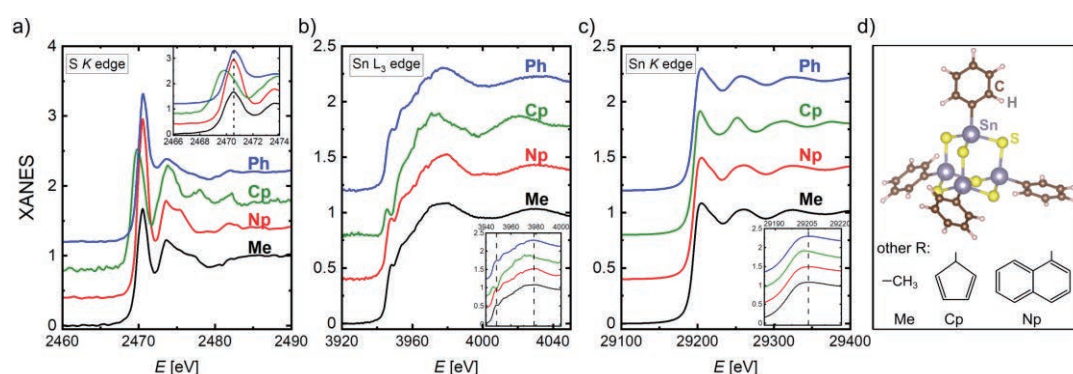

Fig. 1: XANES data for the 4 organotin sulfide samples (Me: black, Np: red, Cp: green, Ph: blue, shifted upwards for clarity) at the S K (a), the Sn L_3 (b) and the Sn K edge (c). The insets highlight the regions close the first maxima of the respective edges. A model of the Ph-Cluster from a DFT simulation[2] is illustrated in (d), along with schematic illustrations of the other organic substituents.

Due to the amorphous nature of the materials, their structural properties, and thereby the apparent origin of this effect, is difficult to determine [3]. Despite these difficulties, our results provide experimental evidence that the nature of the NLO properties is tied to distortions occurring at the cluster core, with almost ideal clusters in compounds that show second harmonic generation, and strongly distorted clusters in the case of compounds that generate a supercontinuum. These distortions may enable a closer proximity of the cluster cores, and thereby influence the NLO response by altering the intermolecular order.

As an example, Figure 1 illustrates the near-edge structure of the absorption spectrum (XANES) around the S K, Sn L_3 and Sn K edges (the latter was measured at P65 of the PETRA-III synchrotron). In all datasets, the edge of the cluster with R=Cyclopentadienyl (Cp) is shifted to lower energies (see insets in Fig. 1), indicating a change in the oxidization state of the cluster core. As we will show in the analysis of the XAFS data, this leads to a significant distortion of the cluster relative to the other compounds.

All in all, the XAFS experiments at the S K edge performed at BL11 of HiSOR provide key information about the potential proximity of neighboring clusters, and therefore contain information on the intermolecular order of the system.

REFERENCES

[1] J.R. Stellhorn et al., in preparation.
[2] N.W. Rosemann et al., Science 6291, 1301 (2016).
[3] B. D. Klee, et al., Phys. Stat. Solidi B 255, 1800083 (2018).
[4] K. Hanau et al., Angew.Chem. Int. Ed. 60, 1176-1186 (2021).

The Local Environment of S in Chalcogenide-Based Solid State Electrolytes by Low-Energy XAFS measurements

Jens R. Stellhorn[a], Shinjiro Hayakawa[a], Pal Jovari[b]

[a] Department of Applied Chemistry, Graduate School of Advanced Science and Engineering,
Hiroshima University, Higashi-Hiroshima, Hiroshima 739-8527, Japan
[b] Wigner Research Centre for Physics, Hungary

Keywords: solid-state electrolyte, glass structure, local structure, EXAFS.

The relationship between the structure, physical and chemical properties of glassy chalcogenides have been intensely investigated for several decades [1, 2]. Ag-doped amorphous chalcogenides can be employed as an electrolyte in the solid state batteries. Although, in principle, many chalcogenide glasses can be used, we have singled out a Ge-Sb-S glass matrix with the composition of $(GeS_2)_{50}(Sb_2S_3)_{50}$, which is non-toxic, a good glass-former and stable in air. We found that Ag-doped Ge-Sb-S alloys form stable amorphous glasses up to 15 at.% of Ag, while higher Ag content leads to the precipitation of Sb crystals. Our recent results [3] show that a small amount of Ag (approx. 2 at. %) increases the ionic conductivity by several orders of magnitude and additional increasing of Ag content results in an exponential increase of ionic conductivity. Ag incorporation also reduces the glass-transition temperature and increases the overall material density, although we have observed that the molar volume of the system is unchanged up to 7 at.% of Ag and changes abruptly after that. As Ag atoms binds mainly to S atoms, the Ag content has a strong impact on the structure of the Ge-Sb-S host matrix. Using Raman spectroscopy, we found that the Ag atoms predominantly attacks $SbS_{3/2}$ structural units in order to form Ag-S and Sb-Sb bonds [3].

To deepen our knowledge on the structural background of ionic conductivity and the changes in the topology of the Ge-Sb-S host matrix, we planned to investigate the local structure in Ge-Sb-S and Ag-Ge-Sb-S glasses around the S atoms using S K-edge (2.47 keV). The bond lengths of Ag-S, Ge-S and
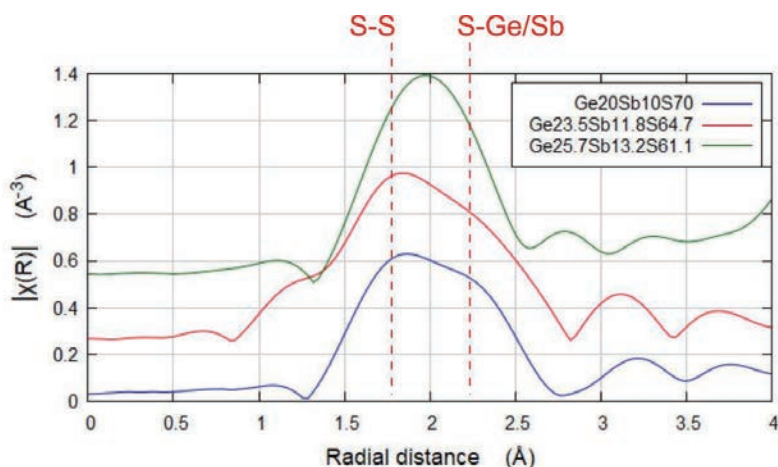

Fig. 1. Fourier transformed magnitudes of the S EXAFS as a function of the S content in the matrix glasses.

Sb-S are well separated (i.e. 2.7 Å, 2.23 Å and 2.45 Å, respectively [4]) and the combination of the resulting EXAFS data with existing X-ray and neutron diffraction structure factors in the framework of reverse Monte Carlo simulation may give reliable models compatible with multiple experimental datasets. As a first result, we show the dependence of the measured signal with the S content in the pure matrix glasses (i.e. without Ag) in Fig. 1. Against the expectation, only two distinct coordinations can be distinguished, which we relate to S-S bonds (signal at lower r) and to bonds between S-(Ge&Sb). The more detailed analysis of the experimental data is now in progress.

We expect that the final experimental results will be crucial for the development of new generation of chalcogenide-based solid state electrolytes.

REFERENCES

[1] A. Zakery, S. R. Elliott, J. Non-Cryst. Solids 330 (1-3) (2003) 1-12.
[2] A.V. Kolobov, Photo-induced Metastability in Amorphous Chalcogenides, Wiley 2003
[3] M. Fraenkl et al. J. Non-Cryst. Solids 499 (2018) 412-419.
[4] I. Pethes et al. J. Alloys Compd 774 (2019) 1009-1016

Quantitative Analysis of Degraded ZnDTP Additive in Engine Oil by Fluorescence yield XAFS method

Susumu MINEOI[a], Kenjiro MOMOSAKI[b], Hirosuke SUMIDA[b], Shinjiro HAYAKAWA[c]

[a]Advanced Automotive Research Collaborative Laboratory, Graduate School of Advanced Science and Engineering, Hiroshima University, 1-4-1 Kagamiyama, Higashi-Hiroshima, Hiroshima 739-8527, Japan
[b]Technical Research Center, Mazda Motor Corporation, 3-1 Shinchi, Fuchu-cho, Aki-Gun, Hiroshima 730-8670, Japan
[c] Graduate School of Advanced Science and Engineering, Hiroshima University, 1-4-1 Kagamiyama, Higashi-Hiroshima, Hiroshima 739-8527, Japan

1.   Introduction
  Various oils used in automobile play important roles in maintaining the power transmission functions and the long-term quality of sliding parts. Therefore, these oils contain various additives to improve required functions while preventing degradation of oils. Zinc dialkyldithiophosphates (ZnDTP) are additives used to reduce wear of sliding parts by forming protective films on the parts surface. In this study, we applied peak fitting method for quantitative analysis of degraded ZnDTP in heat-altered engine oil. To evaluate accuracy of quantitative analysis by peak fitting method, mixture samples of sulfur-containing compounds were measured by using X-ray absorption fine structure (XAFS) method, and the obtained spectra were analyzed by linear combination analysis (LCA) and peak fitting method.

2. Experimental
  Zinc sulfide (ZnS), zinc diethyldithiocarbamate ($[(C_2H_5)_2NCS_2]_2Zn$), octasulfur (S_8), tetramethylthiuram disulfide ($C_6H_{12}N_2S_4$) and calcium sulfate ($CaSO_4$) were used as sulfur-containing compounds in this study. They were mixed with boron nitride (BN) using an agate mortar and pestle, and pelletized in size of 13 mm in diameter and about 0.5 mm in thickness with pellet molding machine. A series of binary mixture was prepared, and the sulfur content in ZnS, $[(C_2H_5)_2NCS_2]_2Zn$, S_8, $C_6H_{12}N_2S_4$ was approximately equivalent to that in $CaSO_4$. They were pelletized with BN in the same manner as described above. A pellet was fixed onto a sulfur-free mending tape placed in a hole of 15 mm in diameter of copper plate of 0.2 mm in thickness.
  Chemical state of sulfur in each sample was investigated using XAFS measurement system at HiSOR BL11 with the X-ray fluorescence method. A sample was placed in a Helium filled sample chamber during the XAFS measurement. The XAFS spectra of pellet samples were acquired with the X-ray energy range from 2460 to 2490 eV with the interval of 0.25eV. The XAFS measurements were repeated 2~4 times, and the obtained spectra were averaged after the normalization with the incident beam intensity. The incident X-ray energy was calibrated so that the main peak energy of potassium sulfate (K_2SO_4) was 2481.6 eV, and the spectrum was measured with the transmission method.
  XAFS spectra of mixture samples were analyzed by using XAFS spectral analysis software Demeter (Athena）[1]. In the peak fitting analysis, the Gaussian function was used to indicate the peak and the arctangent function was used to indicate the excitation energy region where show little difference in absorption due to chemical state. The sigma of Gaussian function and the width of arctangent function were fixed at 1.0 and 0.3, respectively. Two arctangent functions were set up, one for sulfur unreacted with oxygen and the other for sulfur reacted with oxygen, and each center value was fixed at 2475.7 eV and 2482.5 eV, respectively. The heights of the arctangent functions were expected to be equivalent.

3. Results and discussion
  Figure 1 shows sulfur K-edge XAFS spectra of mixture samples and the results of analyses. The results of

LCA were found to be in good agreement with the spectra of the mixture samples. The values in parentheses following the chemical formula are mixing ratio obtained from LCA and peak fitting for each sample. The LCA method is generally known to give accurate quantitative analysis results. Comparing the results of both methods, the peak fitting results differ from LCA result by about 15%. While the LCA requires spectra of the reference compounds constituting the mixture, the peak fitting can be applied even when the reference compounds are not available. For mixture samples similar to those used in this study, it is possible to estimate the mixing ratio by peak fitting analysis, recognizing that it has an error of about 15%.

The sulfur K-edge XAFS spectra of engine oil containing ZnDTP heated under ambient atmosphere at 200°C for up to 40 hours in an electric furnace[2] are shown in figure 2, and the results of peak fitting are shown in Table 1. As with the sulfur-containing compounds described above, two arctangent functions were set up for sulfur unreacted with oxygen and sulfur reacted with oxygen. Although it is necessary to consider that there is an error of about 15%, the analysis results suggest that about 80% of the ZnDTP has undergone oxidation reaction at the time of 40 hours of heating.

The future activities include improving the accuracy of quantitative analysis and promoting the application of this analysis method to other automotive materials as well.

REFERENCES

1. B. Ravel and M. Newville, *Journal of Synchrotron Radiation* 12, 537 (2005)
2. S. Mineoi, K. Momosaki, H. Sumida, S. Hayakawa, *HiSOR Activity Report 2020*, 99 (2021).
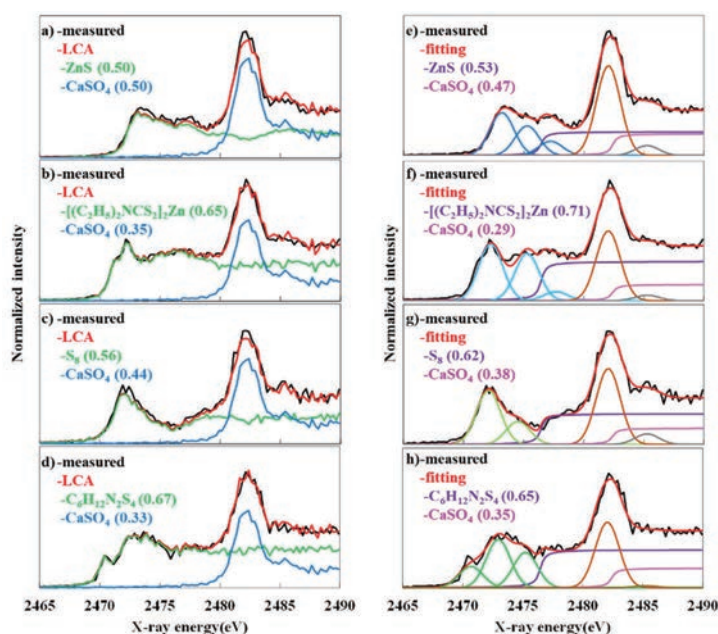
FIGURE 1. Analysis results of sulfur K-edge XAFS spectra, a)~d) : LCA, e)~h) : peak fitting, values in parentheses following the chemical formula are mixing ratio obtained by LCA or peak fitting.
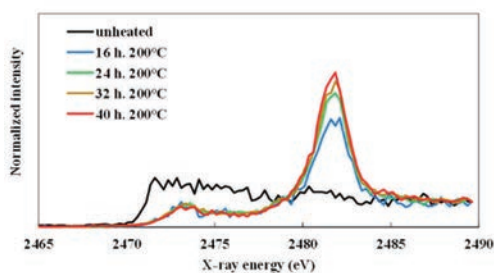

FIGURE 2. Sulfur K-edge XAFS spectra of engine oil samples as a function of the heating time [2].

Table 1. Peak fitting results of XAFS spectra of heat-treated engine oil

Heat-treated Oil Sample	Ratio (peak fitting)	
	Sulfur unreacted with oxygen	Sulfur reacted with oxygen
16 h. 200 °C	0.26	0.74
24 h. 200 °C	0.26	0.74
32 h. 200 °C	0.23	0.77
40 h. 200 °C	0.17	0.83

Hard X-ray absorption spectroscopy of a gold complex included by cyclodextrin

Kiminori Baba [a)], Shinjiro Hayakawa [b)], and Hiroaki Yoshida [a,c)]

[a] Physics program, Graduate School of Advanced Science and Engineering, Hiroshima University, 1-3-1 Kagamiyama, Higashi-Hiroshima, 739-8526 Japan.
[b] Applied Chemistry program, Graduate School of Advanced Science and Engineering, Hiroshima University, 1-4-1 Kagamiyama, Higashi-Hiroshima, 739-8527 Japan.
[c] Hiroshima Synchrotron Radiation Center, Hiroshima University, 2-313 Kagamiyama, Higashi-Hiroshima, 739-0046 Japan.

Keywords: Cyclodextrin, gold, inclusion, potassium, X-ray, absorption

Introduction

Gold recovery using the inclusion of cyclodextrins (CDs) has been proposed as an environmentally friendly method [1]. This method is as simple as mixing $KAuBr_4$ and CD in a 1:2 ratio; α-CD forms gold-containing nanowires that precipitate immediately, whereas β- and γ-CD do not. Crystallographic analysis suggests that the different binding positions of K to CD determine whether nanowire formation occurs or not. To investigate the difference in the binding of K to each CD in aqueous solution, X-ray absorption spectroscopy of the K1s absorption edge was performed at the beamline BL-11 of HiSOR.

Experiment

A mixture of $KAuBr_4$ aq. (20 mM) and CD aq. (40 mM) was prepared and the measurements were carried out on drop-dried films. 20 μl of the solution was dropped onto a potassium-free quartz glass and vacuum dried. This process was repeated five times to obtain a K-containing thin film with sufficient concentration to be used for fluorescence measurement. A special holder was used for the measurement as a solution and the concentration of $KAuBr_4$ aq. was 50 mM. The sample was placed in the He chamber, and synchrotron radiation was incident at an angle of 45° to the normal of the sample. The incident light intensity for normalization was measured by filling the ion chamber with He-N_2 mixed gas.

Results and Discussion

First, solid samples of KCl and KBr were measured for energy calibration (Figure 1). The obtained spectrum of KCl is good agreement with the previous study [2] and the energy axis was calibrated at the Pre-edge peak 3610.2 eV and Post-edge peak 3614.2 eV. Figure 2 shows the spectra of $KAuBr_4$ in film and liquid and a 1:2 mixture of $KAuBr_4$ and α-CD in the film. In the drop-dried film of $KAuBr_4$ aq., K^+ and $AuBr_4^-$ are considered to be ionically bonded and not expected to form molecular orbitals by coordination bonds. Therefore, the K^+ 1s→4p transition appears strongly at 3611.5 eV. On the other hand, the spectrum of $KAuBr_4$@α-CD is similar to that of liquid $KAuBr_4$ due to the coordination of some H_2O to K^+. In Figure 3, the spectra of drop-dried films when various CDs are mixed with $KAuBr_4$ solution. Comparing each spectrum, there is a difference especially in the intensity around 3610 eV. The spectra were fit and separated by the components for each peak and the difference in the peak intensities is discussed in point of the binding of K to each CDs.
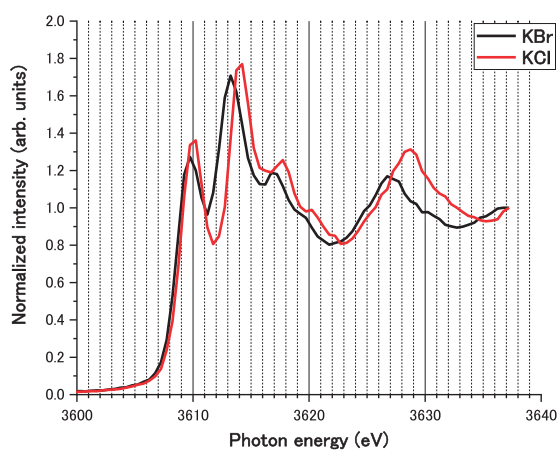
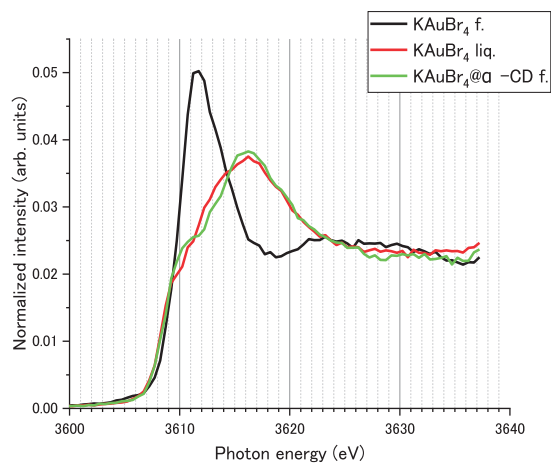Figure 1 XAS spectra of KCl and KBr at the K1s edge.

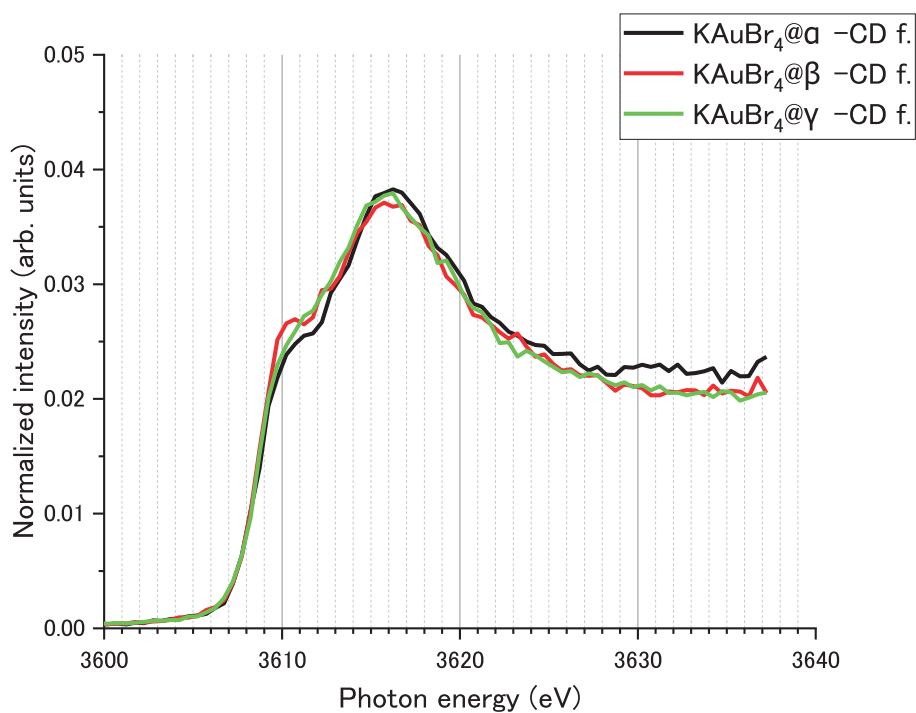Figure 2 XAS spectra of KAuBr₄ (film), KAuBr₄ (liquid), and KAuBr₄@α-CD (film) at the K1s edge.

Figure 3 XAS spectra of KAuBr₄@α-CD, @β-CD, and @γ-CD (film) at the K1s edge.

REFERENCES

[1] Z. Liu et al., *Nat. commun*. **2013**, 1855
[2] W. Li et al., *Geosatand. Geoanal. Res.,* **44** (2020) 805-819

EXAFS of Graphite-Intercalation-Compound $K_{0.64}Ca_{0.36}C_8$

Naohisa Happo[a], Atsushi Kubota[a], Yang Xiaofan[b], Ritsuko Eguchi[b],
Hidenori Goto[b], Mitsuki Ikeda[b], Koji Kimura[c], Koichi Hayashi[c], Shinya Yagi[d],
Shinya Hosokawa[e], Jens R. Stellhorn[f], Shinjiro Hayakawa[f],
and Yoshihiro Kubozono[b]

[a]Graduate School of Information Sciences, Hiroshima City University, Hoiroshima 731-3194, Japan
[b]Research Institute for Interdisciplinary Science, Okayama University, Okayama 700-8530, Japan
[c]Department of Physical Science and Technology, Nagoya Institute of Technology,
Nagoya 466-8585, Japan
[d]Institute of Materials and Systems for Sustainability, Nagoya University, Nagoya 464-8603, Japan
[e]Institute of Industrial Nonomaterials, Kumamoto University, Kumamoto 860-8555, Japan
[f]Graduate School of Advanced Science and Engineering, Hiroshima University,
Higashi-Hiroshima, Hiroshima 739-8527, Japan

Keywords: Graphite intercalation compounds, Superconductivity, XAFS

Metal-doped graphites or graphite intercalation compounds (GIC) have recently garnered much attention owing to their novel physical properties such as superconductivity [1-5]. In 1965, the first GIC superconductor was discovered in K doped graphite, KC_8 [1], and its superconducting transition temperature, T_c, was 0.136 K. The highest value of T_c is now recorded as 11.5 K for CaC_6 at ambient pressure (0 GPa) [2, 3]. In addition to the single element GIC, the binary-elements GIC have been attempted for a realization of higher T_c superconductors. Recently, $K_{1-x}Ca_xC_8$ ($T_c = 6.5 - 11.5$ K) for $0.33 \le x \le 1$ [4] has been successfully prepared by our group, which demonstrates a new rule for the crystal structure of binary-elements GIC that it is exactly determined by the intercalated metal atom with the larger ionic radius. Thus, the X-ray diffraction studies have successfully demonstrated the crystal structures of binary-elements GIC. The structures are categorized as a KC_8-type structure (face-centered orthorhombic, space group No. 70, *Fddd*) [5], a SrC_6-type structure (hexagonal, space group No. 194, $P6_3/mmc$) and a CsC_8-type (hexagonal, space group No. 181, $P6_422$). The KC_8-type structure is realized in $K_{1-x}Ca_xC_8$ [5].

In fact, the crystal lattice was exactly determined, but the actual location of two intercalated metal atoms have yet been elucidated. In other words, it has still been unclear whether an ideal location of metal atoms like solid solution is achieved in the binary-elements GIC. A recent C $1s$ and K $2p$ X-ray photoelectron hologram/spectroscopy of $K_{1-x}Ca_xC_8$ indicated that the cleavage of crystal preferentially occurred at the
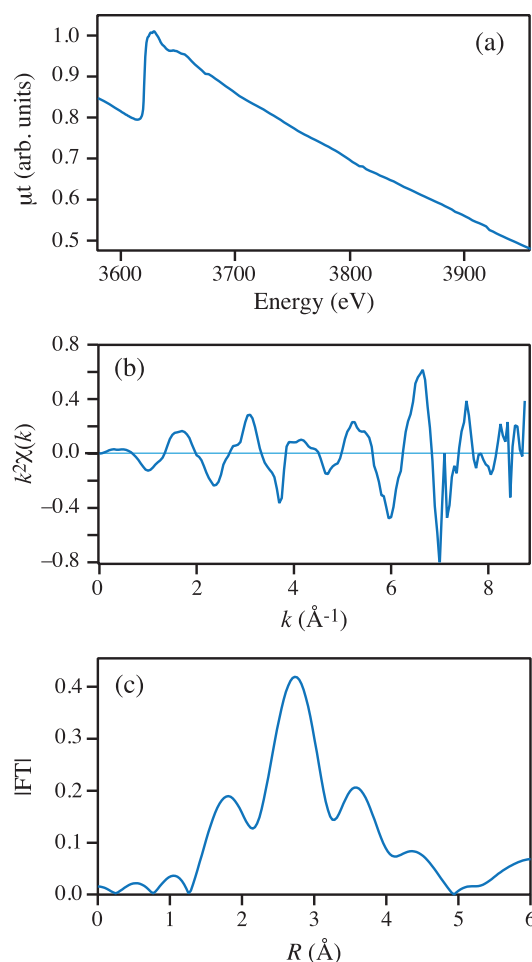

FIGURE 1. K K-edge (a) EXAFS、(b) $k^2\chi(k)$、(c) Fourier transform of $K_{0.64}Ca_{0.36}C_8$

KC_8 layers containing no Ca atoms [6], which differed substantially from the crystal structure indicated from X-ray diffraction (XRD) [5]. This result implies that the phase separation of KC_8 and CaC_6 must be fully explored in the bulk crystals of $K_{1-x}Ca_xC_8$. In this study, to confirm this, an EXAFS experiment was performed.

The K K-edge EXAFS measurements of $K_{0.64}Ca_{0.36}C_8$ were performed at BL-11 of Hiroshima Synchrotron Radiation Center (HiSOR) with transmission mode at room temperature. Samples were sealed with polyester tape in a glove box, quickly introduced into a helium gas displacement chamber.

The K K-edge EXAFS spectra are shown in Fig. 1(a). Fig. 1(b) and (c) show the extracted EXAFS oscillation and the Fourier transform intensity with $k = 3.0 - 9.5$ Å^{-1}, respectively. The main peak around 2.8 Å is considered to be the first coordination K-C. Inverse Fourier transform and curve fitting were performed in R range R = 2.15 - 3.25 Å to analyze the coordination. As a result, the nearest neighbor K-C distance in $K_{0.64}Ca_{0.36}C_8$ is 3.17 Å. K was found to retain, approximately, the KC_8 structure of the base material. We plan to investigate the local structure around the Ca atom in the future.

REFERENCES

1. N. B. Hannay, T. H. Geballe, B. T. Matthias, K. Andres, P. Schmidt, D. MacNair, *Phys. Rev. Lett.* **14**, 225-226 (1965).
2. T. E. Weller, M. Ellerby, S. S. Saxena, R. P. Smith, N. T. Skipper, *Nat. Phys.* **1**, 39-41 (2005).
3. N. Emery, C. Hérold, d'M.Astuto, V. Garcia, C. Bellin, J. F. Marêché, P. Lagrange, G. Loupias, *Phys. Rev. Lett.* **95**, 087003-1-4 (2005).
4. H. T. L. Nguyen, S. Nishiyama, M. Izumi, L. Zheng, X. Miao, Y. Sakai, H. Goto, H. Hirao, Y. Ohishi, T. Kagayama, K. Shimizu, Y. Kubozono, *Carbon* **100**, 641-646 (2016).
5. A. Hérold, D. Billaud, D. Guérard, P. Lagrange, M. E. Makrini, *Physica B* **105**, 253-260 (1981).
6. F. Matsui, R. Eguchi, S. Nishiyama, M. Izumi, E. Uesugi, H. Goto, T. Matsushita, K. Sugita, H. Daimon, Y. Hamamoto, I. Hamada, Y. Morikawa, Y. Kubozono, *Sci. Rep.* **6**, 36258-1-10 (2016).

Kinetics of Denaturation and Renaturation Processes of Double-stranded Helical Polysaccharide, Xanthan in Aqueous Sodium Chloride

Yu Tomofuji,[a] Koichi Matsuo,[b] and Ken Terao[a]

[a]Department of Macromolecular Science, Graduate School of Science, Osaka University, 1-1 Machikaneyama-cho, Toyonaka, Osaka 560-0043, Japan
[b]Hiroshima Synchrotron Radiation Center, Hiroshima University, Kagamiyama, Higashi-Hiroshima, Hiroshima 739-0046, Japan

Keywords: double helix; conformational change; small-angle X-ray scattering; circular dichroism; intermediate state.

Xanthan is a double helical polysaccharide, that is widely used as food additives because of their thickening function [1]. The high viscosity of aqueous xanthan solution is strongly related to the double helical rodlike conformation [2]. Thus, the conformational behavior was extensively studied in a few decades [3]. It is well-known that the renatured conformations depend on the renatured condition, that is, native double helical, hairpin-like, and multibranched structures [4]. In this study, we thus investigated kinetics of denature and renature processes of double helical xanthan to elucidate the mechanism of the aggregating structures [5]. Circular dichroism (CD) and small-angle X-ray scattering (SAXS) measurements were therefore made for xanthan samples with the weight-average molar mass M_w between 340 and 460 kg mol^{-1} in 5 and 10 mM aqueous sodium chloride. This report mainly focuses on the results of CD measurements.
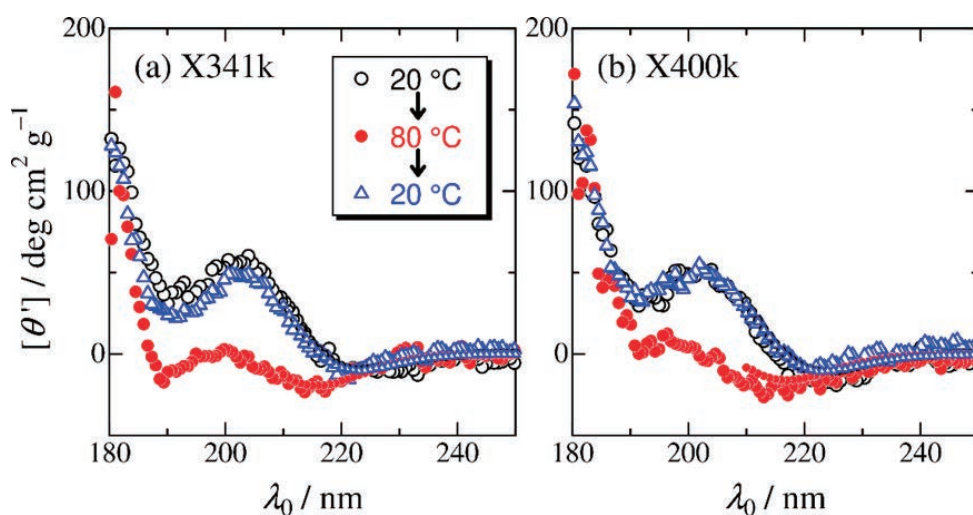

FIGURE 1. CD spectra for (a) X341k and (b) X400k in 10 mM aqueous NaCl. Polymer mass concentration was adjusted around 6 mg mL^{-1}. Black unfilled circles, red filled circles, and blue triangles indicate the data for native sample at 20 °C, denatured sample at 80 °C, and renatured sample (at 20 °C) incubated for 2 days after cooled from 80 °C. Large and small symbols, data from HiSOR and the lab equipment, respectively. Reprinted with permission from ref. [5]. Copyright 2022, Elsevier.

Figure 1 shows the CD spectra, the specific ellipticity $[\theta]'$ plotted against the wavelength λ_0 in vacuum, for X341k and X400k with M_w's being 341 and 400 kg mol^{-1}, respectively. The λ_0 dependence of $[\theta]'$ was

measured between $\lambda_0 = 180$ and 250 nm; the lower limit is due to the absorption of NaCl. The difference in $[\theta]'$ at the two temperatures of 20 °C and 80 °C becomes appreciable between $\lambda_0 = 190$ and 210 nm where the $[\theta]'$ value reflects the conformation of carbonyl groups on the side chains of xanthan.

Time-dependence of $[\theta]'$ at $\lambda_0 = 200$ nm are plotted in Figure 2 after abrupt temperature changes. While the $[\theta]'$ value after the temperature change from 20 °C to 80 °C is almost the same as that for the single chain (red line), those from 80 °C to 20 °C is much slower than that the former temperature change, indicating that the renature process of the side group of xanthan is much slower than the denature process. Interestingly, the main chain conformational change has opposite tendency, that is, only denature process is slower than the temperature change. These results indicate that the conformational change between double helix and single chain of xanthan has at least two steps and an intermediate state with double helical main chain and denatured side groups exist for at most a day after abrupt temperature change. This intermediate state can play an important role for the aggregation structure of xanthan, thus, the rheological properties of xanthan after conformational changes is expected to be controlled by the concentration of xanthan, ionic strength, and temperature changing rate of the renatured process.
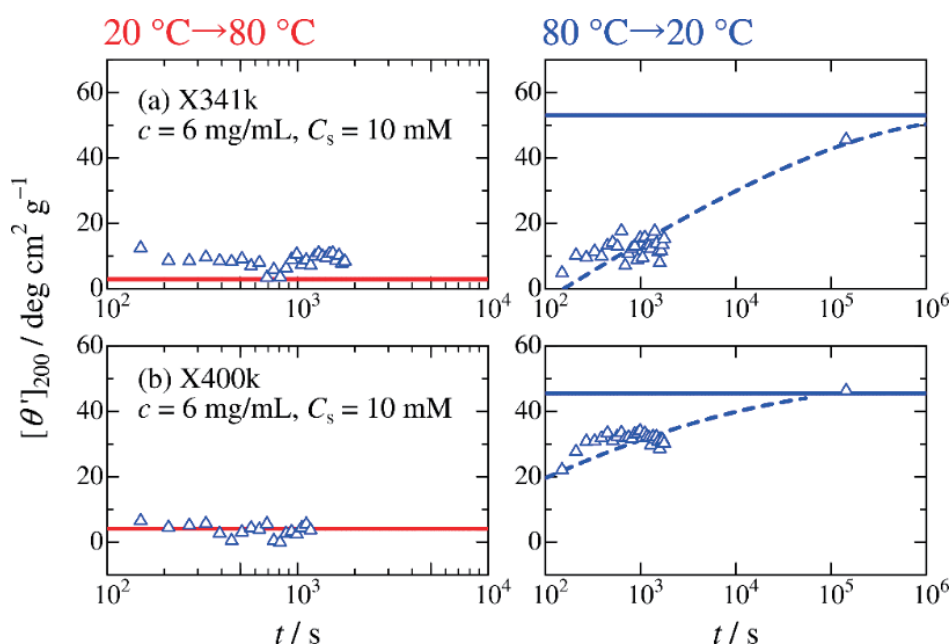

FIGURE 2. Time course of $[\theta']_{200}$ for (a) X341k and (b) X400k in 10 mM aqueous NaCl. Left, abruptly heated from 20 to 80 °C. Right, abruptly cooled from 80 to 20 °C. Solid blue lines, the $[\theta']_{200}$ value for the untreated solution at 20 °C. Reprinted with permission from ref. [5]. Copyright 2022, Elsevier.

This work has been published in Carbohydrate Polymers **275** 118681 (2022).

REFERENCES

1. K. Nishinari, M. Turcanu, M. Nakauma, Y. Fang, *NPJ Sci. Food.* **3**, 5 (2019).
2. T. Sato, T. Norisuye, H. Fujita, *Polym. J.* **17**, 729-735 (1985).
3. E.R. Morris, *Food Hydrocolloids* **86**, 18-25 (2019).
4. Y. Matsuda, Y. Biyajima, T. Sato, *Polym. J.* **41**, 526-532 (2009).
5. Y. Tomofuji, K. Matsuo, K. Terao, *Carbohydr. Polym.* **275** 118681 (2022).

Vacuum Ultraviolet Circular Dichroism Spectra of Helically Aligned Fused Carbon Hollow Nanospheres

Jun Maruyama and Shohei Maruyama

Research Division of Environmental Technology, Osaka Research Institute of Industrial Science and Technology, 1-6-50, Morinomiya, Joto-ku, Osaka 536-8553, Japan

Keywords: Vacuum ultraviolet circular dichroism, Carbon hollow nanosphere, Helical alignment

In our previous study, a cylindrical carbon material with helically aligned nanopores and optical activity was developed [1]. Carbon nanofiber was used as a core of the cylindrical carbon material, onto which polymerized fructose as a carbon precursor and polystyrene nanoparticles as a template for the nanopores were self-assembled with coexistence of sodium alginate to control the assembly. Through heat treatment in an Ar atmosphere, the precursor was converted into carbon walls the polystyrene nanoparticles were decomposed to leave the nanopores. The diffuse reflectance circular dichroism spectra of the carbon material showed positive and negative peaks in the visible light region depending on the helicities.

Considering the application to chiral discrimination and asymmetric synthesis, the mismatch between molecular size and the helical structure of the carbon material (the pore size and the helical pitch was ranging from several 10 to 100 nm) needs to be overcome. Therefore, we attempted to synthesize a new carbon material interacting chiral molecules by reducing the size of the template and the core material and also by using a new carbon precursor and self-assembly techniques [2].
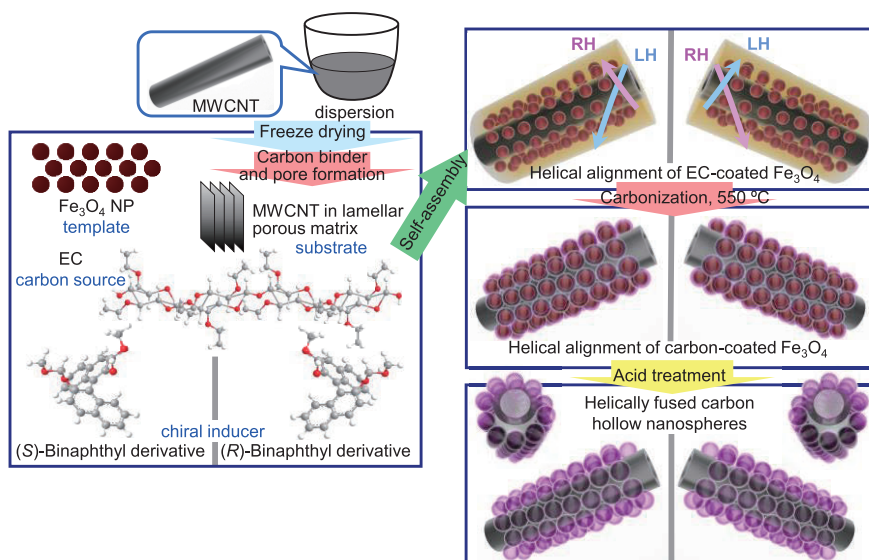

FIGURE 1. Synthesis of helically aligned fused carbon hollow nanospheres (CHNSs) on multi-walled carbon nanotubes (MWCNTs). An aqueous MWCNT dispersion with sodium alginate and poly(ethylene oxide)/poly(propylene oxide) triblock copolymer as a carbon binder precursor and pore-forming agent, respectively, is freeze-dried and heat-treated at 800 °C to form a lamellar porous MWCNT substrate. A mixture of dispersed Fe_3O_4 nanoparticles (NPs), ethylcellulose (EC), and 2,2′-bis(methoxymethoxy)-1,1′-binaphthyl self-assembles on MWCNTs fixed in the lamellar porous matrix. Subsequent heat treatment at 550 °C forms helically aligned fused carbon-coated Fe_3O_4. Acid treatment then removes Fe_3O_4 to obtain CHNSs. The arrows show left-handed (LH) and right-handed (RH) helices. Long-pitch RH and short-pitch LH helices are generated from the mixture with the (*R*)-binaphthyl derivative (right). Long-pitch LH and short-pitch RH helices are generated from the mixture with the (*S*)-binaphthyl derivative (left).

Figure 1 shows a schematic diagram of the carbon material synthesis performed in this study. The core,

carbon precursor, and template were multi-walled carbon nanotube (diameter, 20–40 nm), ethyl cellulose, and Fe_3O_4 nanoparticle (diameter, 5 nm), respectively. A binaphthyl derivative, 2,2′-bis(methoxymethoxy)-1,1′-binaphthyl, was used as a chiral inducer. The carbon materials obtained using (S), (R)-binaphthyl derivatives, and without derivative are labeled C-EC-NP-S-a, C-EC-NP-R-a, and C-EC-NP-a, respectively.

After the carbonization step, the Fe_3O_4 NPs coated with a carbonaceous thin film were helically aligned on MWCNT (Figure 2). The acid treatment removed Fe_3O_4, leaving the CHNSs fused each other.
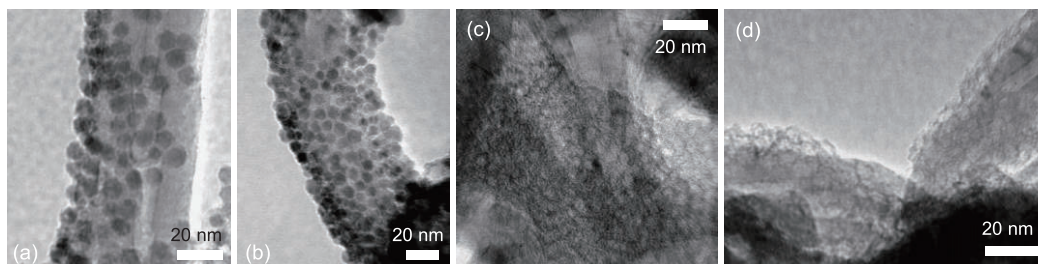

FIGURE 2. TEM images of CHNSs on MWCNTs. CHNSs before (C-EC-NP-S (a), and C-EC-NP-R (b)) and after acid treatment (C-EC-NP-S-a (c), and C-EC-NP-R-a (d)).

Figure 3 shows the vacuum ultraviolet circular dichroism (VUVCD) spectra of C-EC-NP-S-a, C-EC-NP-R-a, C-EC-NP-a, and the MWCNT substrate after the acid treatment (substrate-a). No appreciable CD signals were observed in the spectra of substrate-a and C-EC-NP-a, indicating the absence of helicity or that the RH/LH helicity ratio of each pitch was near unity. In contrast, positive and negative signals exceeding a noise level of ± 0.7 mdeg were observed for C-EC-NP-S-a and C-EC-NP-R-a, respectively. Although the intensities were moderate, these signals demonstrated the chirality of the fused CHNSs on MWCNTs synthesized with the chiral inducer. The correlation between the sign of the CD signal and the helicities of C-EC-NP-S-a and C-EC-NP-R-a was in agreement with those reported previously [1,3]. Despite the low intensity at the CD spectra of C-EC-NP-S-a and C-EC-NP-R-a, the reproducibility was confirmed by the nearly identical spectra for the samples independently synthesized by the same method. The deviation from the mirror-image spectra might be attributable to marginal interaction between the chiral inducer and optically active EC. Numerous CD spectra have been reported for helical silica [4] and Au helical nanostructures [5]. In contrast, CD data for helical carbon materials are limited, and the origins of the CD signals are presently unknown. Further investigations are required to clarify the origins of these signals in helical carbon materials.
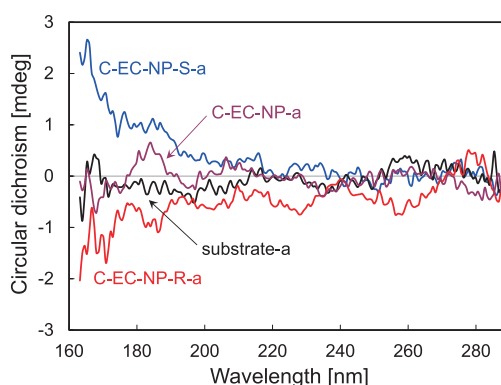

FIGURE 3. CD spectra of substrate-a, C-EC-NP-a, C-EC-NP-R-a, and C-EC-NP-S-a.

REFERENCES

1. J. Maruyama, T. Shinagawa, M. Watanabe, Y. Kashiwagi, S. Maruyama, T. Nagaoka, W. Matsuda, Y. Tsutsui, S. Seki, and H. Uyama, *Small*, **16**, 1905916 (2020).
2. J. Maruyama, S. Maruyama, Y. Kashiwagi, M. Watanabe, T. Shinagawa, T. Nagaoka, T. Tamai, N. Ryu, K. Matsuo, M. Ohwada, K. Chida, T. Yoshii, H. Nishihara, F. Tani, and H. Uyama, *Nanoscale*, **14**, 3748-3757 (2022).
3. S. Liu, Y. Duan, X. Feng, J. Yang, and S. Che, *Angew. Chem. Int. Ed.*, **52**, 6858-6862 (2013).
4. S. Che, Z. Liu, T. Ohsuna, K. Sakamoto, O. Terasaki, and T. Tatsumi, *Nature*, **429**, 281-284 (2004).
5. X. Lan, X. Lu, C. Shen, Y. Ke, W. Ni and Q. Wang, *J. Am. Chem. Soc.*, **137**, 457-462 (2015).

Effect of Sucralose on the Thermal Stability of Myoglobin

Yasuyuki Maki[a], Isamu Kuroiwa[a] and Koichi Matsuo[b]

[a]Department of Chemistry, Faculty of Science, Kyushu University
744 Motooka, Nishi-ku, Fukuoka, 819-0395
[b]Hiroshima Synchrotron Radiation Center, Hiroshima University,
Higashi-Hiroshima 739-0046, Japan

Thermal stability of proteins in aqueous solutions is generally increased by the addition of sugars, which is due to the preferential exclusion of the sugars from the proteins. Recently, we observed that the addition of sucralose (1,6-dichloro-1,6-dideoxyfructose–4-chloro-4-deoxygalactose), the halogenated derivative of sucrose, may decrease the thermal stability of gelatin, a fibrous protein derived from collagen. In this study, we investigated the effect of sucralose on the thermal stability of myoglobin, one of typical globular proteins, by using vacuum-ultraviolet circular dichroism (VUVCD) spectroscopy. VUVCD is an effective tool for analyzing structural change of proteins.

Myoglobin from equine skeletal muscle (Sigma-Aldrich), sucralose (Sigma-Aldrich), and sucrose (FUJIFILM Wako Pure Chemical Corp.) were used without further purification. Phosphate buffer solutions (pH 7.0, 20 mM) with and without sugars were used as solvents. The concentration of sucralose or sucrose was 20 w/v%. Myoglobin was dissolved in the solvents at a concentration of 5 mg/mL. The obtained protein solutions were centrifuged at $16,000 \times g$ for 15 min to remove the aggregates before the measurements. The measurement of VUVCD spectra was performed using the synchrotron-VUVCD spectrophotometer of Hiroshima Synchrotron Radiation Center (BL-12). The CaF$_2$ optical cell with 50 μm path length was used and the spectra were measured from 263 to 175 nm at temperatures from 20 $^{\circ}$C to 85 $^{\circ}$C under a nitrogen atmosphere.

Figure 1 shows VUVCD spectra of myoglobin in the solvents with and without sugars measured at 70 $^{\circ}$C. The spectrum of myoglobin in the phosphate buffer solution showed negative peaks at 208 and 222 nm, indicating the formation of the α-helix structure. The intensity of the peaks of the spectrum was increased by the addition of sucrose, but it was decreased by the addition of sucralose. This result demonstrated that sucrose stabilized the native structure of myoglobin, but sucralose destabilized it.
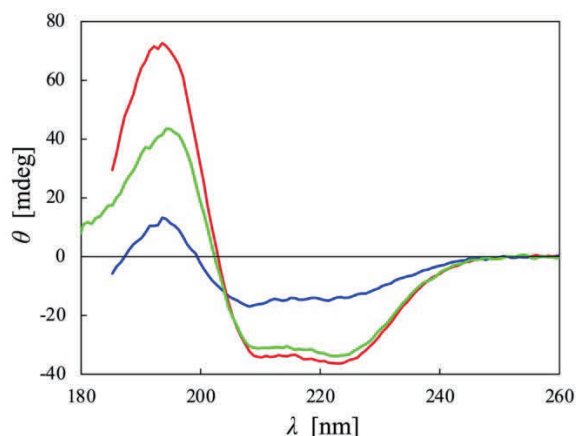

FIGURE 1. VUVCD spectra of myoglobin in 20 w/v% sucralose (blue), 20 w/v% sucrose (red) and phosphate buffer (green) measured at 70 $^{\circ}$C.

Orientation Analysis of Antimicrobial Peptide Magainin 2 Bound to Phospholipid Membrane by Synchrotron-Radiation Linear Dichroism Spectroscopy

Munehiro Kumashiro[a], Ryoga Tsuji[b], Shoma Suenaga[a], and Koichi Matsuo[c]

[a]Department of Physical Science, Graduate School of Science, Hiroshima University, 1-3-1 Kagamiyama, Higashi-Hiroshima, Hiroshima 739-8526, Japan
[b]Physics Program, Graduate School of Advanced Science and Engineering, Hiroshima University, 1-4-1 Kagamiyama, Higashi-Hiroshima, Hiroshima 739-8527, Japan
[c]Hiroshima Synchrotron Radiation Center, Hiroshima University, 2-313 Kagamiyama, Higashi-Hiroshima, Hiroshima 739-0046, Japan

Antimicrobial peptide (AMP) interacts with and induces the damages to the cell membrane of antimicrobial-resistant microorganisms via the complicated mechanisms that remain to be further explored. Recently, we have investigated the interaction mechanism between a model AMP or magainin 2 (M2) and dipalmitoyl-phosphatidylglycerol (DPPG) lipid membrane using a synchrotron-radiation circular dichroism spectroscopy and revealed that α-helix monomers of M2 assembled and transformed into β-strand oligomers with increasing peptide-to-lipid (L/P) molar ratio at 25 °C [1]. However, it is still unclear whether the β-strand oligomers insert into the membrane and are involved in the disruption of cell membrane. In this study, we measured synchrotron-radiation linear dichroism (LD) spectrum of M2 to characterize the orientation of the β-strand oligomers in the membrane.

M2 peptide was synthesized in GL Biochem (Shanghai, China), and DPPG phospholipid was purchased from Avanti Polar Lipids, Inc. Each sample was dissolved in 10 mM phosphate buffer (pH 7.0). DPPG liposome with 100 nm diameter was prepared by an extrusion technique, and then mixed with M2 solution at the L/P molar ratio of 4, which corresponds to the experimental condition mainly occupied by the β-strand oligomeric state [1]. The LD spectrum of M2 in DPPG liposome was measured at BL-12 beamline in HiSOR. The details of the flow LD measurement system are described elsewhere [2].

Figure 1 shows the LD spectrum of M2 in DPPG liposome at L/P = 4. The β-strand oligomers of M2 in the DPPG membranes showed the peak around 200 nm with a small shoulder around 220 nm. According to previous research [3], the net electric or magnetic dipole moments of β-strand around 195 nm and 220 nm are vertical to the strand axis. The β-strand polarized parallel and perpendicular to the membrane normal shows positive and negative LDs at 195 and 220 nm, respectively [3]. Hence, the positive peak LD around 200 nm means that the axis of the β-strands of M2 was parallel to the membrane normal on average, suggesting that the β-strand oligomers of M2 may insert into the membrane and contribute to the formation of pores in the membrane to induce the membrane disruption.

In this symposium, we will discuss the antimicrobial mechanism of M2 based on the paper.

REFERENCES

1. M. Kumashiro and K. Matsuo, *The 25th Hiroshima International Symposium on Synchrotron Radiation*, Hiroshima, Japan, Mar 2021.
2. K. Matsuo, et al., *Proteins* **84**, 349-59 (2016).
3. A. Rodger, et al., *Phys. Chem. Chem. Phys.* **4**, 4051–7 (2002).
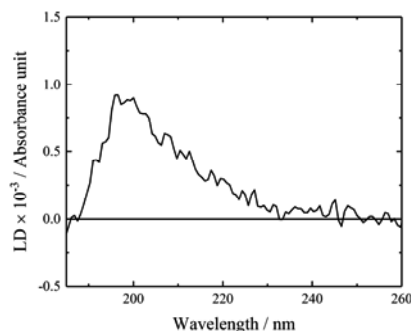4. M. Kumashiro, et al., *Membranes* **12**, 131 (2022).

FIGURE 1. LD spectrum of M2 in DPPG liposome at L/P = 4. The LD was recorded at 25 °C with the flow velocity of 1.0 mL min^{-1}.

Synchrotron Radiation Circular Dichroism Study of Exopolysaccharides from Marine Microbes

Mohamed I. A. Ibrahim[a, b],* Nourhan M. Fathy[c], Mona E. Mabrouk[c], Mohamed M. El-Metwally[c], Hassan H. Ibrahim[b], Koichi Matsuo[a]

[a]*Hiroshima Synchrotron Radiation Center, Hiroshima University, Kagamiyama, Higashi-Hiroshima, Hiroshima 739-0046, Japan.*
[b]*National Institute of Oceanography and Fisheries, NIOF, Egypt.*
[c]*Botany and Microbiology Department, Faculty of Sciences, Damanhur University, Egypt.*

Keywords: Exopolysaccharides, Bacillus Bacteria, Circular Dichroism, Conformation

Marine microbes (*e.g.,* bacteria, fungi, actinomycetes, *etc.*) are promising candidates for production of diverse polysaccharides with several potentials [1, 2]. Three types of polysaccharides were reported (i.e., intracellularly, attached to the cells' surface, or the extracellular polysaccharides (EPS)) [3, 4]. Herein, the research focused on investigating the chemical structure and conformation adopted by a naturally extracted EPS from an isolate of bacillus bacterial species.

First the isolate of the bacillus species was identified using 18S rRNA gene sequence analysis. The optimized conditions for the maximum production of the EPS were developed through studying the effects of several parameters (*e.g.,* temperature, pH, concentration, *etc.*). The produced crude polysaccharides were purified before analysis. The chemical structure of the purified EPS was identified using a complementary different spectroscopic technique (NMR, IR, HPLC, UV, SEC, *etc.*). Then the EPS was subjected to Vacuum Ultraviolet Circular Dichroism (VUVCD) measurements for the conformational study. Different parameters were investigated using VUVCD (*i.e.,* concentration, pH, temperature, and ionic strength).

Identification of the bacillus species isolate involved in EPS production was accomplished genetically and microscopically (data not shown).
The structural analysis based on the NMR, HPLC and SEC chromatography analysis revealed the purified EPS composed of two different molecular weights of neutral homopolysaccharides belong to the Levan-type fructan family. The fructose units were linked together though β-glycosidic linkage (data not shown).
The CD data of this neutral EPS reflected that the conformation of the EPS showed a little dependence on the tested parameters with infinitesimal variations either in the intensity or the chemical shifts of the recorded band in the CD spectrum. The CD spectra of the PS under all tested conditions (*e.g.,* concentration, temperature, and ionic strength) revealed a maximum positive CD band at 178 nm that might be attributed to the $n \rightarrow \pi^*$ transition of ether oxygen (Figure 1). The VUVCD analysis suggested that the EPS in the current study adopts random conformation which was also confirmed by the conventional CD measurement (Congo dye), XRD and UV measurements (data not shown).
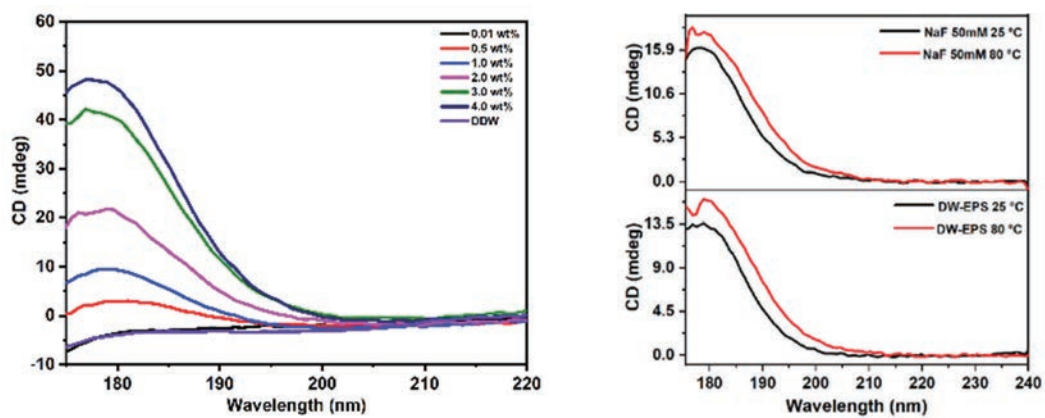
FIGURE 1. Concentration dependence (left), and temperature/ionic strength (right) effects on the conformation of the EPS produced from an isolate of bacillus species.

REFERENCES

1. E. H. Zaghloul and M. I. A. Ibrahim, Front. Microbiol., 13 (2022) Doi: 10.3389/fmicb.2022.903363.
2. L. De Vuyst, B. Degeest, FEMS Microbiol. Rev. 23(2) (1999) 153-77.
3. R.M. Banik, B. Kanari, S.N. Upadhyay, World J. Microbiol. Biotechnol. 16(5) (2000) 407-414.
4. S. Mahapatra, D. Banerjee, Carbohydr. Polym. 97(2) (2013) 627-634.

Interaction Between Liquid Water and Acetone Revealed by Ultraviolet Absorption Spectra

Kazumasa Okada[a], Chika Sugahara[a], and Koichi Matsuo[b]

[a] *Graduate School of Advanced Science and Engineering, Hiroshima University, 1-3-1 Kagamiyama, Higashi-Hiroshima 739-8526, Japan*
[b] *Hiroshima Synchrotron Radiation Center, Hiroshima University, 2-313 Kagamiyama, Higashi-Hiroshima 739-0046, Japan*

Acetone is miscible with water in any ratio, and the binary mixture is a typical aprotic–protic solvent system [1]. The mixture has a negative excess enthalpy in the dilute region [2], indicating that there exists a strong solute–solvent interaction. The acetone molecule plays a role of a hydrogen-bond acceptor. Such an interaction makes its electronic structure somewhat change, causing so-called solvatochromic effects in ultraviolet spectra. Although acetone–water mixture is a typical system, but its systematic, spectrometric studies have not been fully explored yet.

This study focuses on the n–π* absorption band of acetone. The n orbital has a character of the lone-pair electrons on the oxygen atom and these electrons are used to form a hydrogen bond with a hydrogen atom of surrounding water. The magnitude of its peak shift is thus a measure of the strength of interaction. In this respect, the shift of the band has been discussed between gas and aqueous solution, not between liquid and solution. The amount of the experimental shift referred to in theoretical studies varies from around 1500–1600 cm^{-1} [3] to 1700 cm^{-1} [4]. Here we record ultraviolet absorption spectra of aqueous acetone solutions for a series of concentrations of acetone. We are particularly concerned with the absorption in the 210–320 nm region because the peak wavelength of the n–π* transition in pure liquid acetone has been reported to be 274 nm with a molar extinction coefficient of 14 L mol^{-1} cm^{-1} [5].

The experiments were performed on the beamline for vacuum-ultraviolet circular dichroism spectroscopy, BL-12 [6]. The end-station consisted of a chamber for light polarization modulation and a sample chamber for measurements: The schematic diagram was given in Refs. [7, 8]. The chambers were purged with the nitrogen gas rather than evacuated for easy access for sample exchange. The sample cell was composed of a holder assembly made of stainless steel and two CaF$_2$ windows separated by a Teflon spacer ring. The thickness of the spacer defined the optical path length of the cell. All spectra were recorded with a scan speed of 20 nm min^{-1} and a sampling interval of 2.0 s. The spectrum of liquid water was used as a reference. The reference spectrum was measured regularly to compensate for the decrease in the incoming light intensity due to a decay of the ring current. Acetone was obtained commercially from FUJIFILM Wako Pure Chemicals Corp., Japan. The solutions were prepared by mixing gravimetrically acetone with water obtained from a Millipore Direct-Q system.

The peak of the n–π* transition band is hypsochromically shifted upon the dilution of acetone. The peak of the band appears at 272.1 nm for the equimolar mixture. It gradually changes to 261.7 nm in the spectrum of the solution with the molar fraction of acetone, $x_A = 0.05$. The amount of the shift from the peak for pure acetone corresponds to the energy of 20.5 kJ mol^{-1} (or 1710 cm^{-1}). If we assume that the energy of the n^{1}π*^{1} excited state is not affected by the solute–solvent interaction, this energy is considered as the hydrogen-bond energy in the ground state due to the stabilization of the lone-pair orbital of the acetone molecule upon hydrogen-bond formation. The change of the peak position is plotted in Fig. 1, together with the spectra for $x_A = 0.05$ and 0.40.

In the spectra for pure acetone and the solution with $x_A = 0.05$ (blue line in Fig. 1), the n–π* absorption band has a symmetric shape, whereas in the other spectra the band has more or less a tail to shorter wavelengths. The latter is exemplified by the spectrum in pink line in Fig. 1. The widths at a half maximum are 29.3 nm on the shorter wavelength side and 22.0 nm on the longer side. This fact suggests a mixed

solution structure with different fractions of components, ranging from fully hydrated acetone to hydration-shared complexes, to acetone clusters: In shared hydration, water molecules are involved in the hydration shell of two or more acetone molecules simultaneously. We are planning to conduct the multivariable analysis for deducing the components and fractions.

We are grateful to the staff of the Hiroshima Synchrotron Radiation Center for stable operation of the storage ring.
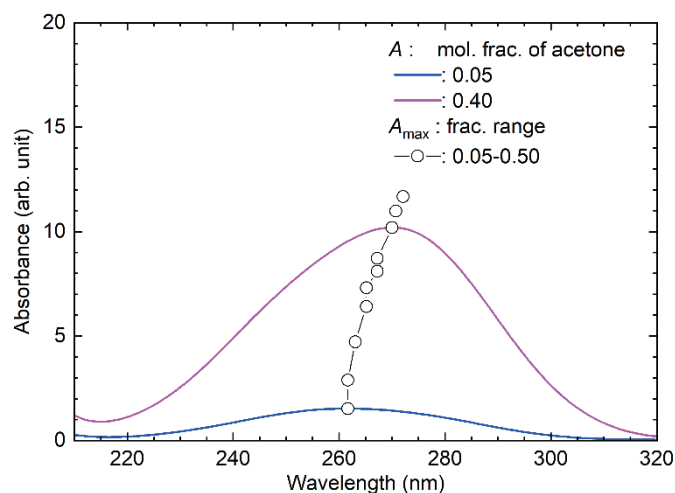

FIGURE 1. The n–π* absorption band of acetone in aqueous solutions. The blue and pink lines show the bands for samples with the molar fraction of acetone of $x_A = 0.05$ and 0.40, respectively. The open circles are the peak positions for samples with $x_A = 0.05$–0.50.

REFERENCES

1. A. J. Parker, *Quart. Rev. Chem. Soc. (London)* **16,** 163–187 (1962).
2. B. Löwen and S. Schulz, *Thermochim. Acta* **262,** 69–82 (1995).
3. K. Aidas, J. Kongsted, A. Osted, K. V. Mikkelsen, and O. Christiansen, *J. Phys. Chem. A* **109,** 8001–8010 (2005).
4. F. Grozema and P. Th. van Duijnen, *J. Phys. Chem. A* **102,** 7984–7989 (1998).
5. M. Hesse, H. Meier, and B. Zeeh, "Spectroscopic Methods in Organic Chemistry, 2nd Ed." Georg Thieme Verlag (2008), Chapter 1.
6. M. Sawada, H. Namatame, and M. Taniguchi, *J. Phys.: Conf. Ser.* **425,** 162010 (2013).
7. N. Ojima, K. Sakai, T. Fukazawa, and K. Gekko, *Chem. Lett. (Jpn.)*, 832–833 (2000).
8. K. Matsuo, T. Fukuyama, R. Yonehara, H. Namatame, M. Taniguchi, and K. Gekko, *J. Electron Spectrosc. Relat. Phenom.* **144-147,** 1023–1025 (2005).

Desiccation-Induced Conformational Change of Peptide in the presence of Membrane Characterized by Vacuum-Ultraviolet Circular Dichroism Spectroscopy

Shun Sawada[a], Munehiro Kumashiro[b], Ryota Imaura[c], and Koichi Matsuo[d]

[a] Faculty of Science, Hiroshima University
[b] Graduate School of Science, Hiroshima University,
[c] Graduate School of Advanced Science and Engineering, Hiroshima University
[d] Hiroshima Synchrotron Radiation Center, Hiroshima University

Keywords: circular dichroism, G3LEA protein, secondary structure, trehalose, membrane, water, phase transition

Elucidating the molecular mechanisms of cell desiccation tolerance is necessary for engineering the biological stability of mammalian cells in dry state and for developing countermeasures against foodborne illnesses caused by dry foods. Recent studies have reported that organisms, including sleeping chironomid, survive severe dehydration via accumulating saccharides and proteins, such as trehalose and group 3 late embryogenesis abundant (G3LEA) protein, inside their cells [1-3]. Although the trehalose protects cell structure and function via the well-understood mechanisms of water replacement and glass formation, the molecular mechanism of desiccation protection by the G3LEA protein remains to be further explored. In this study, to characterize the desiccation protection mechanism of G3LEA protein, we measured vacuum-ultraviolet circular dichroism (VUVCD) spectra of two tandem repeats of 11-mer consensus motif of G3LEA protein in the presence of lipid membranes under aqueous and dry conditions. We also investigated the conformation of G3LEA peptide in the presence of trehalose to reveal the synergistic effect of G3LEA protein and trehalose on the desiccation protection.

Native G3LEA peptide shows a negative peak CD at 200 nm, which is characteristic for random coil structure of proteins. The spectral shapes of G3LEA peptide in DMPC, DMPG, and POPC liposomes were consistent with that of native G3LEA peptide, indicating that G3LEA peptide did not interact with liposomes in aqueous solution. G3LEA peptide in DMPC liposome in dry state shows two negative peaks around 222 and 208 nm and a positive peak at 190 nm, which are characteristic for α-helix structure of proteins. This indicates that the formation of α-helix in G3LEA peptide contributes to its desiccation preservation function. Further, the peak intensities of VUVCD spectra of G3LEA peptide in DMPG liposome is about 2-fold greater than that in DMPC liposome, implying the importance of electrostatic interaction between positively charged residues of G3LEA peptide and negatively charged headgroups of phospholipid membrane. Further, we found that the spectral intensities of G3LEA peptide in DMPC liposome in the presence of trehalose was 4-fold greater than that in the absence of trehalose. These results suggest that G3LEA protein protects cell structure by interacting with the headgroups of phospholipid membranes, and that trehalose enhances the desiccation protection function of G3LEA protein.

REFERENCES
1. Juliana Sakamoto Yoneda, Andew J.Miles, Ana Paula Ulian Araujo, and B.A. Wallace , Differential dehydration effects on globular proteins and intrinsically disordered proteins during film formation , Protein Sci   Vol.26 pp718-726(2017)
2. Daixi Li ,and Xiaoming He ,Desiccation Induced Structural Alterations in a 66-Amino Acid Fragment of an Anhydrobiotic Nematode Late Embryogenesis Abundant (LEA) Protein ,Biomacromolecules Vol.10   No.6   pp1469-1477(2009)
3. Takao Furuki, Takahiro Watanabe, Tadaomi Furuta, Kiyoshi Takano, Ryo Shirakashi , and Minoru Sakurai, The Dry Preservation of Giant Vesicles Using a Group 3 LEA Protein Model Peptide and Its Molecular Mechanism, Bull.Chem.Soc.Jpn. Vol.89 No.12 pp1493-1499(2016)

Soft X-ray Polarization Measurements of Phospholipid Multilayers Supported on Hydrophilic Si Surfaces

Masataka Tabuse[a], Akinobu Niozu[a], and Shin-ichi Wada[a,b]

[a]*Graduate School of Advanced Science and Engineering, Hiroshima University*
[b]*Hiroshima Synchrotron Radiation Center, Hiroshima University*

Keywords: Linear Polarization, XAS (X-ray absorption spectroscopy), NEXAFS (near edge X-ray absorption fine structure), Phospholipids, DCCP, DOPC.

Lipid membranes supported on substrates are promising systems for use in biological sensing, biocompatibility, bioelectronics [1]. The idea that ordered lipid molecules can be prepared by several convenient methods, like freeze-thaw and spin-coating methods [2]. We also confirmed that the phospholipid multilayers made by simple dripping of acetone solution onto hydrophilic Si substrates under atmospheric pressure and moisture and room temperature conditions forms well-ordered multilamellar structures. But the quality of ordering as well as formation process of ordered lamellar structure during such a short period is not well understood.

X-ray absorption spectroscopy (XAS) is one of powerful tools to investigate local structural and dynamical information because of its element selectivity. Especially, one can easily get orientation structure around X-ray absorption center by using linearly polarized X-ray beam. In this study, polarization dependence of XAS measured for phospholipid multilayers supported on hydrophilic Si surfaces was investigated in order to quantify the orientation quality.

Measurements of near edge X-ray absorption fine structure (NEXAFS) have been performed at BL-13 of HiSOR, where is a soft X-ray beamline with a Dragon-type spherical grating monochromator developed to investigate soft X-ray spectroscopy for surface organic materials. During measurements, the experimental chamber had a base pressure less than 1×10^{-9} Torr. NEXAFS spectra around the C K-edge were recorded in total electron yield (TEY) mode by measuring a sample drain current by changing incident angle of synchrotron radiation. Polarization at BL-13 is horizontal due to bremsstrahlung from a bending magnet and the polarization factor P was determined to be 0.95 [3] by measuring azimuthal angle-dependent NEXAFS spectra of a highly oriented pyrolytic graphite (HOPG) [4].

DPPC and DOPC phospholipid molecules were used to form supported lipid membranes from 10 to 1000 multilayer by changing the dripping volume of lipid solution onto hydrophilic Si substrates, and moreover for getting the bilayer membranes, multilayers on substrates were considerably washed by immersing Milli-Q water. DPPC and DOPC molecules are shown in Fig. 1, consisting of a polar zwitterionic hydrophilic group and two non-polar carbon chains. So, molecules in aqueous solution form bilayers with the carbon chains facing each other due to hydrophobic interaction. It is understood that bilayers of DPPC with saturated carbon chains form crystalline-like gel phase at room temperature, while DOPC with unsaturated chains composes liquid crystalline phase. Fig. 2 shows typical polarization dependent NEXAFS spectra measured for (a) DPPC and (b) DOPC on Si surfaces at C K-edge. Although DPPC shows clear polarization dependence, the dependence of DOPC in not so dominant. Tendency of such polarization dependence does not depend on the layer number of lipids. So, the different degree of
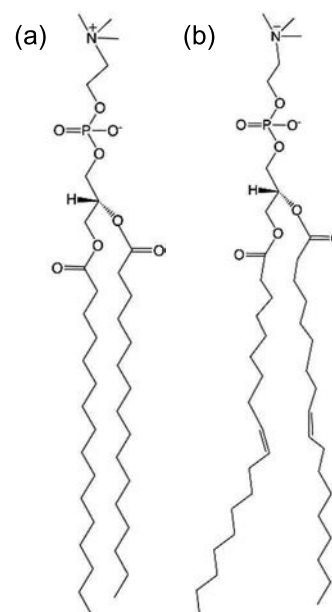

FIGURE 1. Molecular structures of phospholipids (a) DPPC and (b) DOPC.
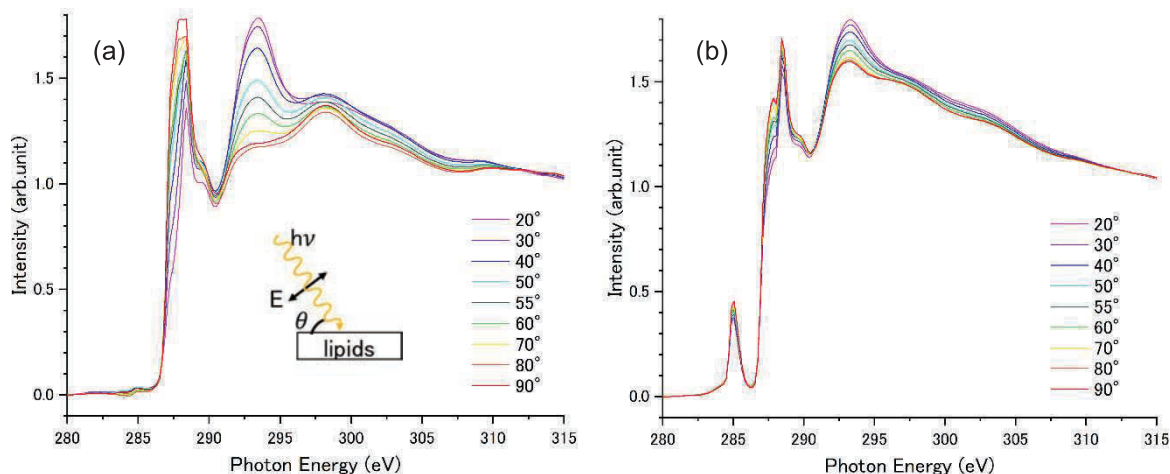
FIGURE 2. Polarization dependent NEXAFS spectra of (a) DPPC and (b) DOPC phospholipids multilamellar membranes measured at C K-edge. These membranes consist of about 100 bilayers, which are confirmed by simple molar consideration and interference of reflected visible light. Incident angle θ from the surface, and therefore the angle of electric vector from the surface normal, is defined like inset.

polarization dependence reflects not only the orientation angles themselves but also the different phase (ordering quality) of lipid membranes. On the basis of above consideration and the careful analysis of polarization dependence of each resonant peaks, DPPC bilayers (that is gel phase) consist of 60% ordered component and 40% non-ordered one, while DOPC bilayers (liquid phase) contain 80% non-ordered carbon chains. This is the first quantitative analysis of phospholipid bilayers of DPPC and DOPC by means of strong advantage of polarization quality and element selectivity of soft-X ray synchrotron radiation.

REFERENCES

1. Z.Zhi, I.Y. Hasan, A. Mechler, *Biotechnol. J.* **13**, 1800101 (2018).
2. A.C. Simonsen and L.A. Bagatolli, *Langmuir* **20**, 9720-9728 (2004).
3. M. Tabuse, K. Yamamoto, S. Wada, *HiSOR Activity Report 2019*, 124 (2020).
4. B. Watts, L. Thomsen and P.C. Dastoor, *J. Electron Spectrosc. Relat. Phenom.* 151, 208 (2006).

Characterization of self-assembled monolayers of methyl-ester terminated naphthalenethiol

A. Niozu[a], H. Sunohara[b], S. Tendo[a], M. Tabuse[a], and Shin-ichi Wada[a,c]

[a]*Graduate school of advanced science and engineering, Hiroshima University, Higashi-Hiroshima 739-8526, Japan*
[b]*Faculty of science, Hiroshima University, Higashi-Hiroshima 739-8526, Japan*
[c]*Hiroshima Synchrotron Radiation Center, Hiroshima University, Higashi-Hiroshima 739-0046, Japan*

Keywords: Self-assembled monolayers (SAMs), Near edge X-ray absorption fine structure (NEXAFS)

Core-electron excitations by soft X-ray radiation possess several unique properties that differ from those of valence excitations. Core-excitation energy depends on the element and its chemical environment, which allows selective excitation of a specific atom in a molecule. In general, core excitation is followed by Auger decay on a time scale of a few femtoseconds, resulting in final states with large excess energy. Thereafter, the excited molecule follows a rich variety of relaxation pathways, e.g. desorption of ion and neutral species and charge transfer within the molecule.

An interesting phenomenon that reflects the selective nature of core excitation is site-selective bond breaking of molecules, i.e. the so-called "molecular scalpel" [1,2]. In particular, it has been reported that highly site-selective bond scission can be achieved in self-assembled monolayers (SAMs) of molecules absorbed on metal surfaces [1,2]. Furthermore, our recent experiments on aliphatic and aromatic SAMs have suggested that the degree of site-selective bond scission depends on the molecular structure of backbone between the excitation cite and the metal substrate. This implies the key role of energy transfer between the excitation cite and the substrate for the manifestation of site-selective bond scission. To corroborate this picture, a systematic experimental study about the fragmentation dynamics dependent on the molecular structure is helpful.

In this study, we investigated the ion desorption dynamics of SAMs of methyl-ester terminated naphthalenethiol molecules. The SAM samples were prepared by immersing Au substrates in 1.0 mM benzene solution of the sample molecules for 24 hs. We characterized the prepared SAM samples by near-edge X-ray absorption fine structure (NEXAFS) measurements. The experiment was performed at the BL 13 of HiSOR. The C K-edge NEXAFS spectra were measured by the total electron yield (TEY) method via the sample drain current. The measurements were performed at different incident beam angles, and polarization dependence of the NEXAFS intensity was investigated. The obtained NEXAFS spectra (Fig. 1) show peaks corresponding to excitations to individual unoccupied molecular orbitals and provided precise values of their excitation energies. In addition, the spectra exhibit a clear polarization dependence, which supports the formation of well-oriented SAMs on the substrate.

The measurements of desorbed ions were performed at BL 2B of photon factory (PF) in KEK. PF was operated in the hybrid operation mode, and the single-bunch component of the X-ray beam was skimmed and used in the experiment. Partial ion yield (PIY) spectra were recorded with a time-of-flight ion spectrometer. The PIY of CH_n^+ (n=0,1,2,3) ions showed a prominent enhancement at the $C1s(OCH_3) \rightarrow \sigma^*(O-CH_3)$ resonant excitation, which have been observed in previous experiments on methyl-ester terminated SAMs [1,2]. From the PIY spectra, we evaluated the degree of site-selective desorption by analyzing the relative yield of CH_n^+ ions. The degree of site-selectivity for the present molecule with naphthalene backbone was evaluated to be between those for molecules with benzene and biphenyl (with two benzene rings) backbones. The present results corroborate the correlation between the molecular conductivity and the site selectivity in ion desorption.
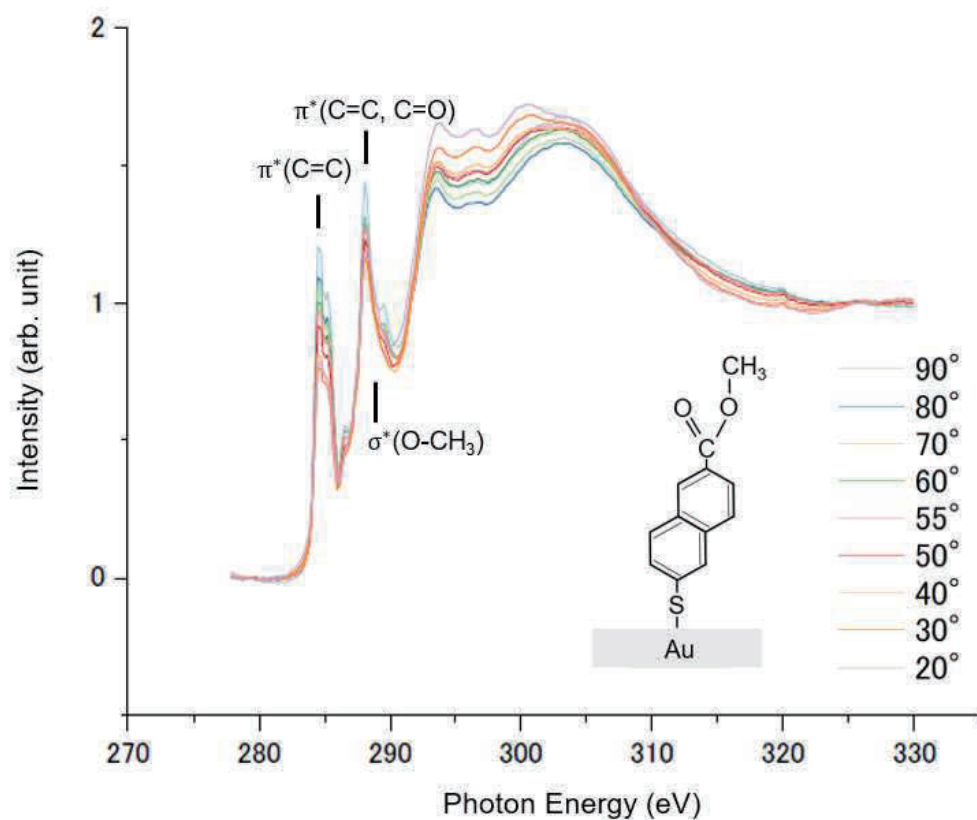
FIGURE 1. TEY spectra for methyl-ester terminated naphthalenethiol SAMs. The spectra exhibit peaks corresponding to excitations to individual π^* and σ^* orbitals. The spectra show a clear polarization dependence, which supports the formation of ordered SAMs on the Au substrate.

REFERENCES

1. S. Wada, H. Kizaki, Y. Matsumoto, R. Sumii, and K. Tanaka, J. Phys. Condens. Matter **18**, 1 (2006).
2. S. Wada, and K.Tanaka, J. Mass Spectrom. Soc. Jpn **58**, 17 (2010).

C K-edge XAFS measurements for detection of unsaturated bonds in organically bridged silica materials

Shinjiro Hayakawa [a], Joji Oshita[a,b], Kei Oshima[a,b], Shogo Tendo[c],

Toshinori Tsuru[d], Shinichi Wada[c]

a *Applied Chemistry program, Graduate School of Applied Science and Engineering,, Hiroshima University, Higashi-Hiroshima, Hiroshima 739-8527, Japan*
b *Smart Innovation program, Graduate School of Applied Science and Engineering,, Hiroshima University, Higashi-Hiroshima, Hiroshima 739-8527, Japan*
c *Physics program, Graduate School of Applied Science and Engineering,, Hiroshima University, Higashi-Hiroshima, Hiroshima 739-8526, Japan*
d *Chemical Engineering program, Graduate School of Applied Science and Engineering,, Hiroshima University, Higashi-Hiroshima, Hiroshima 739-8527, Japan*

Introduction

Microporous organosilica membranes are attractive because of unique features such as a high surface area, improved hydrothermal stabilities, and applications of them are widely expanding [1]. Most of researches have been focused on bis-(triethoxysilyl)ethane (BTESE) and characteristics of BTESE derived materials. To expand the possibilities of organosilica membranes we have been exploring different precursors to introduce ethylene and acetylene bridges into the organosilica membranes. Though the properties of the synthesized organosilica were characterized by the many analytical methods, there exists no method that provide the evidence of the unsaturated carbon bond. Moreover, the quantification of the amount of the unsaturated bonds is quite difficult. We have utilized C K-edge XAFS spectroscopy for detecting remained unsaturated bonds in PMOs, and the possibilities of quantification will be discussed.

2. Experimental

2.1 Samples

Table 1 shows precursors used for synthesis of organically bridged silica materials. Three types of precursor were utilized including bis-(triethoxysilyl)ethane, bis-(triethoxysilyl)ethylene and bis-(triethoxysilyl)acetylene, and their ethoxysil groups were converted into siloxane or silanor groups via the hydrolysis and polymerization. Ethanol solutions of samples (5 wt %) were prepared for each, and a 30 μL of the solution was dropped three times onto a Si substrate of approximately 15 mm square under atmospheric condition.

TABLE 1.   Samples and their precursors of the organically bridged silica materials investigated.

Sample name	Precursor	Approximate mass fraction of carbon
BTES-E1 ethane bridge	$(EtO)_3SiCH_2CH_2Si(OEt)_3$	18.17 %
BTES-E2 ethylene bridge	$(EtO)_3SiCHCHSi(OEt)_3$	18.45 %
BTES -E3 acetylene bridge	$(EtO)_3SiCCSi(OEt)_3$	18.74 %

2.2 XAFS measurements

Experiments were carried out on the beamline BL13 [2]. Incident X-rays were monochromatized with a grating monochromator, and the incident X-ray intensity was monitored from a Au coated grid of stainless steel. The beam size at the sample position was approximately 1 mm square, and the glancing angle of 20 deg. was employed for X-ray absorption fine structure (XAFS) measurements. Total electron yield (TEY) from a sample was monitored, and the normalized spectra were utilized for the further analysis. To avoid the inhomogeneity of the sample on the substrate, several positions on the sample were selected for measurements. Incident X-ray energy was calibrated with the main peak obtained with PMMA, and the observed spectra were shifted to 1.44 eV minus to let the peak energy of PMMA be 288.34 eV.

3. Results and discussion

Figure 1 shows C K-edge XAFS spectra of organically bridged silica materials. Obtained main peak with ethane bridged silica material (BTES-E1) showed a main peak around 290.2 eV, and the spectrum was almost identical to that obtained with the blank (Si substrate). On the other hand two spectra of ethylene bridged silica material (BTES-E2) showed the characteristic peak around 285.04 eV. The peak energy was similar to the reported value of 1s to π^* transition (around 285 eV) obtained from the adsorbed ethylene on the Si substrate [3]. Though the similar peak corresponding to 1s to π^* transition was expected with acetylene bridged silica, no clear peak was observed while the broadened peaks remained in the present experiment. It was clear that the direct evidence of the remaining unsaturated carbon bond in the organically bridged silica material could be monitored with the C K-edge XAFS spectroscopy. While the contribution of the surface contamination with the hydrocarbon should be considered for determination of the portion of the unsaturated bond in the sample.
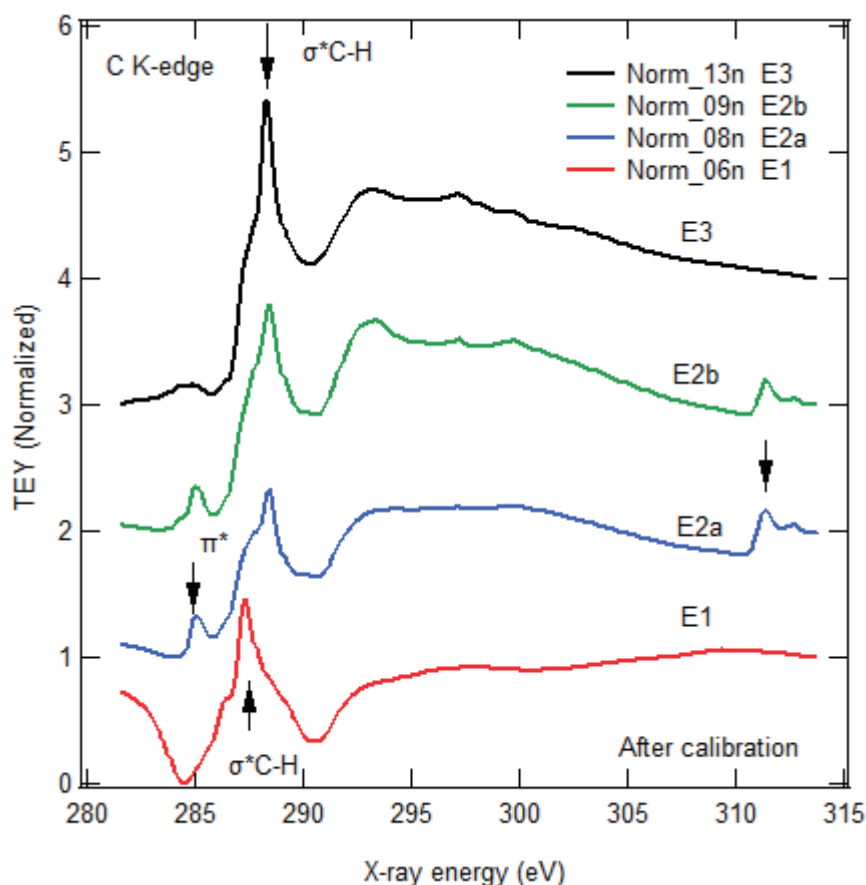
REFERENCES

1. R. Xuet al., Appl. Mater. Interfaces 6(2014) 9357-9364.
2. S. Wada et al., Surf. Sci. 601 (2007) 3833-3837.
3. F. Matsui et al., Surf. Sci. 401 (1998) L413-419.

NEXAFS Study of Fullerene Adsorbed on Aminothiophenol Self-Assembled Monolayer

K. Kono[a], S. Wada[b,c] and T. Sekitani[b,c]

[a]*Faculty of Science, Hiroshima University*
[b]*Graduate School of Advanced Science and Engineering, Hiroshima University*
[c]*Hiroshima Synchrotron Radiation Center, Hiroshima University*

Keywords: fullerene, self-assembled monolayer, NEXAFS

Controlling the microstructure of organic materials to nanometer scale has motivated scientific studies of molecular structure and molecular interactions on various surfaces. Among the various techniques for the preparation of ordered thin organic films, the self-assembled films provide the desired control of molecular order at the interface and also introduce various functional groups into the molecular systems with a high degree of control over the orientation of those groups. The adsorption of thiols onto gold surfaces has attracted considerable interest, as it has been shown that such adsorption can result in formation of well-organized self-assembled monolayer (SAM) [1]. The organothiol self-assembly on metal surface have attracted much interest in a facile manipulating of surface functionality. The SAM have successfully employed as components in molecular electronic devices. Self-assembly of aromatic thiols are particularly interesting due to the interaction of delocalized π orbital of phenyl ring.

The unique electronic, spectroscopic, and structural properties of fullerene and fullerene derivative are very useful to the various application of the material. C_{60} is characterized by the delocalized and highly degenerate orbitals due to π bonding and I_h symmetry. C_{60} is also served as an excellent electron acceptor in molecularly designed donor-acceptor systems, such as molecular photovoltaics [2]. Attachment of C_{60} to the tail groups of SAM provides discrete monolayers of C_{60} and also organized assembly where C_{60} will remain immobilized on the surface.

In this study, the adsorbed state of C_{60} on SAM was examined by NEXAFS spectroscopy. 4-aminothiophenol was used as SAM. The aminothiophenol SAM was prepared by immersing the gold coated Si substrate to 1 mM solution in ethanol for 24 h. The aminothiophenol SAM was cleaned with ethanol and dipped further in 1 mM C_{60} solution in benzene and kept for 24 h. The SAMs thus formed were washed with benzene, ethanol, and dichloromethane. C_{60} multilayer was formed by dropping benzene solution to gold coated substrate and drying in air. NEXAFS measurements were performed at BL13 of Hiroshima Synchrotron Radiation Center.

C K-edge NEXAFS spectra were measured for C_{60}, aminothiophenol SAM and C_{60} adsorbed aminothiophenol SAM. Since NEXAFS spectrum of C_{60} adsorbed SAM includes contribution of aminothiophenol, the component of C_{60} in the C_{60}-SAM was obtained by subtraction of aminothiophenol SAM spectrum from C_{60}-SAM spectrum. The obtained difference spectrum shows similar feature as C_{60} spectrum, but shows peak shifts and peak broadening compared with C_{60} spectrum. Particularly, LUMO peak is shifted to higher photon energy and overlapped with LUMO+1 peak. A higher photon energy shift of LUMO is observed at C_{60} adsorbed on 11-amino-1-undecane thiol SAM [3]. The results suggest that C_{60} is chemisorbed on amino thiolate SAM by hybridization between N Pz of amino group and π^* orbital of C_{60}.

REFERENCES

1. J. C. Love, L. A. Estroff, J. K. Kriebel, R. G. Nuzzo, G. M. Whitesides, *Chem. Rev.* **105**, 1103 (2005)
2. H.Imahori, Y.Kashiwagi, T. Hasebe, M. Kimura, T. Hanada, Y. Nishimura, I. Yamazaki, Y. Araki, O. Ito, S. Fukuzumi, *Thin Solid Films*. **451-452**, 580 (2004)
3. A.Patnaik, K.Okudaira, S.Kera, H.Setoyama, K.Mase, N.Ueno, *J. Chem. Phys.* **122**, 154703 (2005)

Magnetic property of transition metal phosphides interface of Ni_xP/Fe_2P

Naoyuki Maejima[a,b], Yuma Kuwabara[a], Edamoto Kazuyuki[a,b] and Masahiro Sawada[c]

[a]*Rikkyo University*
[a] *Coll. Sci., Rikkyo Univ., Tokyo 171-8501, Japan*
[b]*Research Center for Smart Molecules, Rikkyo Univ.,Tokyio 171-8501, Japan*
[c]*Hiroshima Synchrotron Radiation Center, Hiroshima University*

Fe_2P is ferromagnetic material which exhibits a first-order magnetic phase transition at 216 K[1] and promising candidates for magnetic refrigerant materials. $(Fe_{1-x}Ni_x)_2P$ exhibit ferromagnetic properties at room temperature for x < 0.8. The Curie temperature decreases with increasing x and it exhibit a Pauli paramagnet behavior for x>0.5. [2] The Curie temperature can be controlled by adjusting the ratio of Fe and Ni. Additionally, experimental and computational studies suggest that the magnetism of $(Fe_{1-x}Ni_x)_2P$ involves mainly the Fe sites and little or no Ni sites. [3]

Recently, we have succeeded in fabricating Ni phosphide thin films on Fe_2P substrates. In generally, surfaces and interfaces often exhibit different magnetic properties from those in the bulk. It is interesting that the new magnetic properties will appear or not in this transition metal phosphide thin film and interface, however there is few reports about the magnetic properties of this kind of materials. here has been no study of the magnetic properties at the interfaces of such phosphide thin films. In this study, we investigated the magnetic properties of the thin films and interfaces of Ni_xP/Fe_2P samples using X-ray magnetic circular dichroism (XMCD) measurements.

$Fe_2P(10\text{-}10)$ were cleaned by cycles of Ar^+ ion spattering (0.5 keV) and annealing (600°C and 750°C, respectively). The cleaned surfaces showed c(2x2) LEED patterns. Ni atoms were deposited on the Fe_2P clean surface at 500°C, which induces phosphorization of the film owing to surface segregation of P atoms from the bulk.[4] The thickness of thin film was controlled by amount of Ni deposition. Prepared Ni_xP/Fe_2P samples exhibit c(2x2) LEED pattern. The XMCD measurement of $Fe_2P(10\text{-}10)$ and $Ni_2P(10\text{-}10)$ clean surfaces and Ni_xP/Fe_2P thin film samples were performed at BL14 of HiSOR at room temperature.

Fig. 1(a) and (b) show the Fe L edge and Ni L edge XMCD spectra obtained from the Ni_xP/Fe_2P sample. The film thickness was estimated 5Å. The Fe Ledge XMCD signal obtained from the substrate of the thin film sample was significantly increased from that of clean Fe_2P substrate sample. Ni phosphides such as Ni_2P, Ni_3P, and NiP_3 are paramagnetic,[5] and Ni_2P substrates did not show XMCD signals (as shown in Fig.1(d)), Ni_xP/Fe_2P samples showed XMCD signals at the Ni L edge. The peak top energy of the Fe L_3 edge of the thin film sample is lower than that of the Fe_2P clean surface and the peak top energy of the Ni L_3 edge of the thin film sample is higher than that of Ni_2P clean surface. Figure 2 shows Fe L edge XMCD spectra obtained from NixP/Fe2P samples of various film thicknesses. Thickness dependence of XMCD signal was confirmed. These results indicated that the interaction between the thin film and the substrate changed the Curie temperature of the substrate and magnetic property of Ni phosphide thin film.
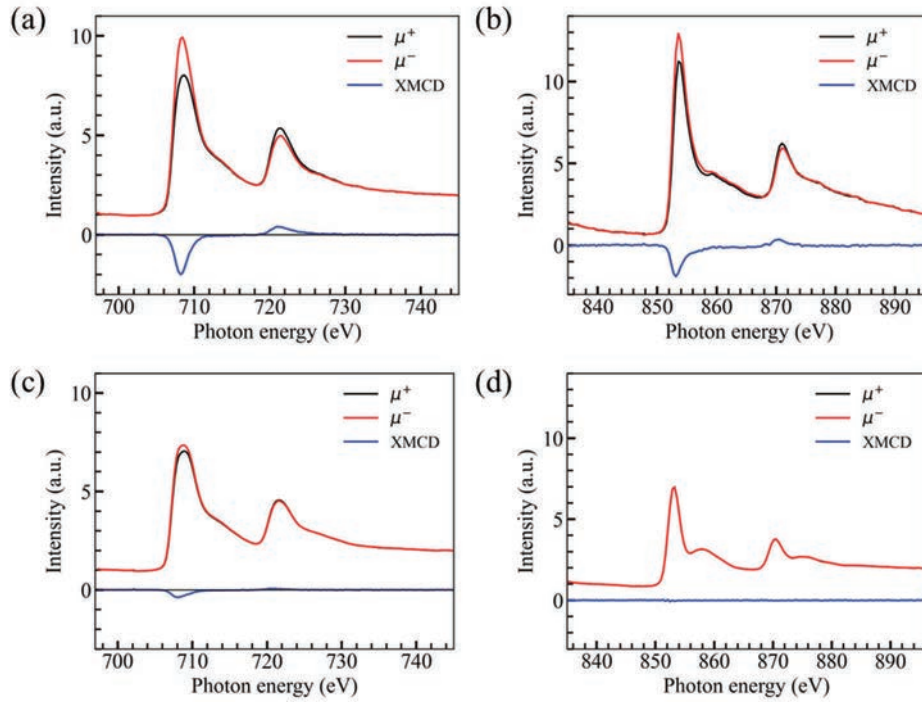
FIGURE 1. (a) Fe L edge and (b) Ni Ledge XMCD spectra measured from Ni_xP/Fe_2P sample. XMCD spectra from (c)Fe_2P and (d)Ni_2P clean surface were measured as reference sample.
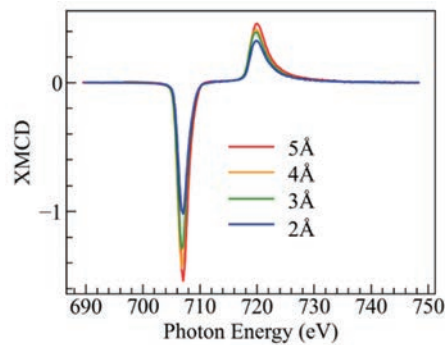

FIGURE 2. Fe L edge XMCD spectra obtained from Ni_xP/Fe_2P samples of various film thicknesses.

REFERENCES

[1] L. Lundgren *et al.,* Phys. Scr., **17** (1978) 39.
[2] J. B. Goodenough *et al., J. Appl. Phys*. **40** (1969) 3.
[3] R.Zachnetal *et al., J. Alloys Compd.* **383** (2004) 325
[4] Y. Sugizaki *et al.*, *Jpn. J. Appl. Phys.* **57** (2018) 115701.
[5] K. Zeppenfiled *et al*., *J. Phys. Chem. Solids* **54**, (1993) 1527.